Role of glutamine synthetase in angiogenesis beyond glutamine synthesis

Guy Eelen[1,2]*, Charlotte Dubois[1,2]*, Anna Rita Cantelmo[1,2&], Jermaine Goveia[1,2], Ulrike Brüning[1,2$], Michael DeRan[3], Gopala Jarugumilli[3], Jos van Rijssel[4], Giorgio Saladino[5], Federico Comitani[5], Annalisa Zecchin[1,2], Susana Rocha[6], Hongling Huang[1,2†], Saar Vandekeere[1,2], Joanna Kalucka[1,2], Christian Lange[1,2‡], Francisco Morales-Rodriguez[1,2], Bert Cruys[1,2], Lucas Treps[1,2], Leanne Ramer[1,2#], Stefan Vinckier[1,2], Katleen Brepoels[1,2], Sabine Wyns[1,2], Joris Souffreau[1,2], Luc Schoonjans[1,2], Wouter H. Lamers[7], Yi Wu[8], Jurgen Haustraete[9,10], Johan Hofkens[6], Sandra Liekens[11], Richard Cubbon[1,2,¶], Bart Ghesquière[1,2], Mieke Dewerchin[1,2], Francesco L. Gervasio[5,12], Jaap D. van Buul[4], Xu Wu[3] & Peter Carmeliet[1,2]

(1) Center for Cancer Biology, University of Leuven, Leuven, B-3000, Belgium; (2) Center for Cancer Biology, VIB, Leuven, B-3000, Belgium; (3) Cutaneous Biology Research Center, Massachusetts General Hospital, Harvard Medical School, Charlestown, Massachusetts 02129, USA; (4) Department of Molecular Cell Biology, Sanquin Research and Landsteiner Laboratory, Academic Medical Centre, University of Amsterdam, 1066CX Amsterdam, the Netherlands; (5) Department of Chemistry, University College London, London WC1E6BT, UK; (6) Molecular Imaging and Photonics, University of Leuven, Leuven, B-3000, Belgium; (7) Tytgat Institute for Liver and Gastrointestinal Research, Academic Medical Center University of Amsterdam, 1105BK Amsterdam, The Netherlands; (8) Center for Cell Analyses and Modelling, University of Connecticut Health Centre, Farmington 06032, USA; (9) Inflammation Research Center, VIB, Ghent, B-9000, Belgium; (10) Department of Biomedical Molecular Biology, Ghent University, Ghent, B-9000, Belgium; (11) Department of Microbiology and Immunology, University of Leuven, Leuven, B-3000, Belgium; (12) Institute of Structural Molecular Biology, University College London, London WC1E6BT, UK. Present affiliations: (&) Université de Lille, INSERM U1003, Physiologie Cellulaire, F-59000 Lille, France; ($) Max-Delbrück-Center for Molecular Medicine, 13092 Berlin, Germany ; (†) Immunology Department, St. Jude Children's Research Hospital, Memphis 38105, USA; (‡) DFG-Research Center for Regenerative Therapies, Technical University Dresden, 01307 Dresden, Germany; (#) Department of Biomedical Physiology and Kinesiology, Simon Fraser University, Burnaby V5A 1S6, Canada; (¶) Division of Cardiovascular and Diabetes Research, Multidisciplinary Cardiovascular Research Centre, University of Leeds, Leeds LS29JT, U.K. *equal contribution

<u>Editorial correspondence</u>: P. Carmeliet, M.D., Ph.D.
         Laboratory of Angiogenesis and Vascular Metabolism
         Center for Cancer Biology, VIB
         Dept. Oncology, KU Leuven
         Campus Gasthuisberg O&N4, Herestraat 49-912,
         B-3000, Leuven, Belgium
         phone: 32-16-32.30.39
         e-mail: peter.carmeliet@kuleuven.vib.be

SUMMARY (150 WORDS)

Glutamine synthetase (GS) converts glutamate and NH_4^+ to glutamine. GS is expressed by endothelial cells (ECs), but surprisingly shows negligible glutamine synthesizing activity at physiological glutamine levels. Nonetheless, genetic loss of *GS* in ECs impairs vessel sprouting during vascular development, while pharmacological GS blockade suppresses angiogenesis in ocular and inflammatory skin disease, only minimally affecting healthy adult quiescent ECs. This relies on inhibition of EC migration but not proliferation. Mechanistically, GS knockdown (GS^{KD}) reduces membrane localization and activation of the GTPase RHOJ, while activating other Rho GTPases and Rho kinase (ROCK), thereby inducing actin stress fibers and impeding EC motility. ROCK inhibition rescues the GS^{KD} EC migratory defect. Notably, GS is auto-palmitoylated and interacts with RHOJ to sustain RHOJ palmitoylation, membrane localization and activation. These findings highlight a novel molecular activity for GS, in addition to its glutamine synthesizing activity, in EC migration during pathological angiogenesis.

INTRODUCTION

Endothelial cells (ECs) line the lumen of blood vessels. Emerging evidence reveals that EC metabolism controls vessel sprouting (angiogenesis)[1-3]. While glutamine catabolism in ECs was recently characterized[4], it remains undetermined if glutamine anabolism controls angiogenesis *in vivo*. Glutamine is a carbon and nitrogen donor for biomolecule production and is involved in redox homeostasis. Most cells take up glutamine (the most abundant amino acid in the blood) and thus do not need to synthesize it. Nonetheless, certain cell types express glutamine synthetase (*GS*; also called glutamate-ammonia ligase; *GLUL*), the enzyme capable of *de novo* glutamine production from glutamate and ammonia in an ATP and Mg^{2+}/Mn^{2+} requiring reaction. GS serves also another biochemical function, i.e. ammonia clearance, but

64   this is best described for hepatocytes, astrocytes and muscle. ECs also express GS[5], though

65   its role and importance in angiogenesis remain unknown. Since ECs are exposed to high

66   plasma glutamine levels, it is puzzling why these cells express GS. Global *GS* deficiency

67   causes embryonic lethality, presumably due to the inability to detoxify ammonia[6]. *GS* defi-

68   ciency in humans is extremely rare and leads to multi-organ failure with infant death[7]. If and

69   how GS affects angiogenesis has never been analyzed. Here we characterized the role and

70   importance of GS in vessel sprouting.

RESULTS

71

VESSEL SPROUTING REQUIRES ENDOTHELIAL GS

72

73   We checked GS expression in endothelial cells of the retinal microvasculature with a genetic

74   *GS* reporter mouse (*GS*[+/GFP] mice with a nucleus-targeted *GFP-lamin A* fusion reporter

75   transgene in the GS ORF of one allele[6]). GFP tracing in the postnatal day 5 (P5) retinal plex-

76   us, co-stained with the endothelial cell marker Isolectin B4 (IB4; red), revealed endothelial ex-

77   pression of GFP (and thus of GS) in the microvasculature (Fig. 1a).

78   Human umbilical venous endothelial cells (further referred to as "ECs") expressed *GS*

79   to similar levels as human colon ECs, liver ECs, human umbilical arterial ECs and blood out-

80   growth ECs (BOECs), but to a lower level than lung ECs (Extended Data Fig. 1a). However,

81   GS expression in ECs or isolated mouse liver ECs (mLiECs) was lower than in HEPG2 hepa-

82   tocellular carcinoma cells or astrocytes (Extended Data Fig. 1a-c), known to highly express

83   GS. Glutamine withdrawal (below physiological concentration of 0.6 mM) increased GS pro-

84   tein levels in ECs (Fig. 1b; Extended Data Fig. 1b), as previously documented for other cell

85   types[8].

We intercrossed $GS^{lox/lox}$ mice with two different EC-specific tamoxifen inducible Cre driver lines, i.e. *VE-cadherin(PAC)-Cre*^{ERT2} and *Pdgfb-Cre*^{ERT2} mice to obtain respectively GS^{vECKO} and GS^{pECKO} mice. Correct recombination of the loxed *GS* allele was confirmed (Extended Data Fig. 1d-e) and caused an average 84% reduction of *GS* mRNA levels in mLiECs isolated from GS^{vECKO} mice (Fig. 1c). In the neonatal retina, vascular plexi in P5 GS^{vECKO} mice showed hypobranching and reduced radial expansion, whereas vessel coverage by $NG2^+$ pericytes and vessel regression (number of empty collagen IV^+ sleeves) were unaffected (Fig.1d-h, Extended Data Fig. 1f,g). However, the number of filopodia at the vascular front and of distal sprouts with filopodia, both parameters of EC migration, was lower in GS^{vECKO} pups (Fig 1i-j). Furthermore, the complexity of the vasculature at the utmost leading front of the plexus was decreased as determined by counting the number of branches in distal sprouts (Extended Data Fig. 1h). In contrast, quantification of $IB4^+$ EdU^+ cells revealed no difference in the number of proliferating ECs (Fig. 1k-m; Extended Data Fig. 1i). Hypobranching was also observed in the dorsal dermal blood vasculature in E16.5 GS^{vECKO} embryos (Fig. 1n-r). A similar retinal phenotype was observed in GS^{pECKO} mice (Extended Data Fig. 1j-m). Thus, loss of endothelial GS causes vascular defects by impairing EC migration but not proliferation.

The retinal vascular defect restored over time (Extended Data Fig. 1n-u) and at 6 weeks, GS^{vECKO} animals (with *GS* deleted in ECs at P1-P3) did not show overt vascular defects (Extended Data Fig. 1v-ag). GS^{vECKO} animals gained normal body weight, and blood biochemistry and hematological profiles were normal at 6 weeks (Extended Data Table 1). Vascular restoration may relate to the possibility that homozygous mutant ECs were outcompeted over time by residual wild type ECs, in which recombination did not occur (as documented in mice with endothelial loss of other key metabolic genes[9]) or because of other compensatory

adaptations. Alternatively, the results raise the question if the effect of endothelial GS loss may be larger in growing (motile) ECs during vascular development than in quiescent (non-motile) ECs during adulthood in healthy conditions.

We then explored if pharmacological blockade of GS with methionine sulfoximine (MSO), which irreversibly blocks its catalytic activity, reduced pathological angiogenesis. First, in the oxygen-induced model of retinopathy of prematurity (ROP)[2,3], treatment of pups with MSO reduced the formation of pathological vascular tufts (Fig. 2a-c), while modestly increasing the vaso-obliterated area (Fig. 2d and Extended Data Fig. 1ah-ai). Second, we used the corneal micro-pocket assay (CPA) in mice with slow-release basic fibroblast growth factor (bFGF) containing pellets as a model of corneal neovascularization. Inclusion of MSO in the pellet reduced formation of new CD31$^+$ blood vessels in the otherwise avascular cornea (Fig. 2e-g). Finally, we used the imiquimod-based mouse model of inflammation-driven skin psoriasis and found a remarkable dose-dependent reduction of the CD105$^+$ EC area upon topical treatment of the affected skin with MSO (Fig. 2h-l). Thus, pharmacological GS blockade inhibits pathological angiogenesis in the inflamed skin and in several eye disorders.

SILENCING GS REDUCES EC MIGRATION

We then used *GS* knockdown (GS^{KD}) ECs (shRNA-mediated; >80% silencing; Extended Data Fig. 2a) in *in vitro* spheroid sprouting assays to assess vessel sprouting. GS^{KD} reduced the number of sprouts per spheroid and the total sprout length (Fig. 3a,b,e,f). Re-introduction of a shRNA resistant *GS* (rGS^{OE}) rescued the sprouting defect (Extended data Fig. 2b-c). The sprouting defect in GS^{KD} spheroids was maintained upon mitotic inactivation of ECs with mitomycin C (MitoC) (Fig. 3c-f), further suggesting an EC motility defect. In agreement, at physiological glutamine levels, GS^{KD} did not affect EC proliferation (Fig. 3g). The sprouting defect

133   was also not due to reduced EC viability or increased oxidative stress, or to changes in ener-

134   gy charge, glutathione or NADPH levels, glycolysis, glucose or glutamine oxidation, or oxygen

135   consumption (Extended Data Fig. 2d-m).

136   GS^{KD} impaired migration in scratch-wound and Boyden chamber assays, even upon

137   MitoC treatment, an effect that was rescued by re-introducing a shRNA-resistant *GS* (rGS^{OE})

138   (Fig. 3h-i). Furthermore, sparsely seeded GS^{KD} ECs had a reduced velocity of random

139   movement (Fig. 3j; Supplemental movies 1 and 2) and a decreased lamellipodial area (Fig.

140   3k-m). Comparable results were obtained with a second non-overlapping shRNA and a *GS*-

141   specific siRNA (Extended Data Fig. 2a; Extended Data Fig. 3a-e).

142   The migration defects suggested that GS^{KD} perturbed the remodeling of the actin cyto-

143   skeleton, necessary for cellular motility. Notably, we detected an increase in F-actin levels in

144   GS^{KD} ECs (Fig. 3n). A role of GS in cytoskeletal remodeling was further suggested by analyz-

145   ing repolymerization of the actin cytoskeleton upon disruption with the F-actin polymerization

146   inhibitor latrunculin B and subsequent wash-out. Latrunculin B perturbed the normal morphol-

147   ogy of control and GS^{KD} ECs (Fig. 3o-r). After wash-out, when control cells had rebuilt a nor-

148   mal actin cytoskeleton, GS^{KD} ECs still had higher F-actin levels, mainly originating from in-

149   creased numbers of stress fiber bundles (Fig. 3s-u). GS^{KD} did not alter α-tubulin levels (Fig.

150   3v; Extended data Fig. 4a-h).

151   The increase in F-actin levels was also present in ECs, freshly isolated from MSO-

152   treated mice (Extended data Fig. 4i-k), and in confluent GS^{KD} ECs aligning a scratch wound *in*

153   *vitro* (Extended data Fig. 4l-n). Confluent monolayer GS^{KD} ECs displayed compromised junc-

154   tional integrity (Extended data Fig. 4o-v). Functionally, this corresponded to a decrease in

155   trans-endothelial electrical resistance (TEER) of GS^{KD} ECs *in vitro* (Extended data Fig. 4w)

156   and increased leakiness of inflamed (but not healthy) vessels *in vivo* (Extended data Fig. 4x-
157   z).

158

GLUTAMINE PRODUCTION BY ENDOTHELIAL GS

160   To explore whether the migration defect was attributable to reduced *de novo* glutamine syn-
161   thesis, we measured the glutamine synthesizing activity of GS by supplementing ECs with
162    $^{15}NH_4Cl$ (Extended Data Fig. 5a). At a physiological concentration of 0.6 mM glutamine or
163   higher, the glutamine producing activity of GS was negligible, approximating the level ob-
164   served in ECs treated with MSO; it slightly increased only upon glutamine withdrawal, pre-
165   sumably to compensate for the lack of available glutamine (Fig. 4a). Similar results were ob-
166   tained in medium containing dialyzed serum (Extended Data Fig. 5b). For further details see
167   Supplementary Discussion 1 and Extended Data Fig. 5c-n.

168   To determine if the GS[KD] phenotype relied on the catalytic site of GS, we used previ-
169   ously reported concentrations of MSO[10], which competes with glutamate in the catalytic site of
170   GS and irreversibly blocks GS. MSO reduced EC spheroid sprouting, impaired EC migration
171   in scratch-wound assays upon MitoC treatment, decreased lamellipodial area, while increas-
172   ing F-actin levels after latrunculin B wash-out but without affecting EC proliferation (Extended
173   Data Fig. 5o-t). Even though other (off-target) effects of pharmacological GS inhibition cannot
174   be formally excluded, MSO phenocopied the *GS* knockdown, suggesting that the catalytic site
175   of GS is indispensable to control EC cytoskeletal homeostasis.

GS INHIBITION AFFECTS RHOJ ACTIVITY

177   Small GTPases and their effectors control F-actin levels and motility[11], thus we explored if

178   Rho GTPases were downstream targets of GS. We focused on RHOJ, since it is EC-

179   enriched[12], and blocking endothelial RHOJ was proposed to be a novel anti-angiogenesis ap-

180   proach[13]. Of note, RHOJ[KD] ECs fully phenocopied GS[KD] ECs in terms of decreased mobility

181   and barrier function (data not shown).

182   Since RHOJ localizes to plasma and organelle membranes to become activated[14] and

183   RHOJ is almost exclusively detected in the membrane fraction[15], we explored if GS levels

184   regulated RHOJ's membrane localization and activity. Immunoblotting revealed that RHOJ

185   was only detectable in the membrane fraction of ECs (consistent with previous findings[15]),

186   and that GS[KD] decreased the amount of RHOJ in the membrane fraction (without concomitant

187   increase in the cytosolic fraction, possibly because of proteasomal degradation[16]) as well as

188   the levels of active RHOJ (Fig. 4b,c). GS[KD] did not overtly affect *RHOJ* transcript levels (rela-

189   tive mRNA levels: 0.99 ± 0.03 in control *vs* 0.85 ± 0.05 in GS[KD]; n=3, p<0.05).

190   We also explored if GS[KD] affected other Rho GTPases in ECs. We focused on the

191   RHOA/B/C – Rho kinase (ROCK) – myosin light chain (MLC) axis, as silencing of endothelial

192   RHOJ increases signaling of this pathway and induces aberrant F-actin stress fiber formation

193   through an as yet undefined mechanism[13,17] (Fig. 4d). Standard GST-Rhotekin pull-down as-

194   says showed that GS[KD] increased the activity of RHOA and RHOC, but not of RHOB (Fig. 4e-

195   g). Of note, GS[KD], much like other stimuli, increased total RHOB levels. We confirmed the in-

196   crease in RHOA activity at the individual cell level with a DORA-RHOA-FRET biosensor (Fig.

197   4h; Extended Data Fig. 6a), and observed that the abnormally elevated RHOA activity in re-

198   tracting lamellipodia in GS[KD] ECs evoked more numerous, but smaller and more short-lived

199   lamellipodia (Fig. 4i), which could contribute to the motility impairment. As suggested previ-

200   ously[18], increased RHOA activity in lamellipodia locally leads to actomyosin contraction

201   through ROCK and pMLC, thereby prematurely retracting the lamellipodium. Combining GS[KD]

202   and RHOJ[KD] did not further increase RHOA activity (data not shown) confirming that RHOJ

203   silencing by itself increased RHOA activity and suggesting that GS indeed primarily acts via

204   RHOJ to control RHOA signaling.

205   Downstream of Rho GTPases, GS[KD] and MSO-treated ECs had elevated ROCK1 and

206   ROCK2 protein levels (Fig. 4j), and enhanced ROCK activity, as determined by pMLC protein

207   levels, which were similarly induced in GS[KD] and RHOJ[KD] ECs (Fig. 4k; Extended Data Fig.

208   6b-n). In agreement, ROCK inhibitors (Y27632, fasudil hydrochloride and H1152 dihydrochlo-

209   ride (not shown)) rescued the GS[KD] phenotype (Fig. 4l-o; Extended Data Fig. 6o-w) whereas

210   myosin light chain kinase (MLCK) inhibitors (ML7; peptide 18) did not (Extended Data Fig. 6x-

211   aa), suggesting that MLC phosphorylation through ROCK rather than MLCK is more important

212   in mediating the GS[KD] phenotype in ECs. Thus, GS[KD] lowers membrane localization and ac-

213   tivity of RHOJ, while activating RHOA, RHOC, and ROCK.

214   We explored with which of these Rho GTPases GS interacted, assuming that such an

215   interaction might facilitate / be necessary for their activation, nonetheless keeping in mind that

216   RHOJ can negatively regulate the activity of the RHOA/ROCK/MLC axis[13,17] and hence that

217   loss of a primary interaction of GS with RHOJ could indirectly explain the elevated levels of

218   RHOA/ROCK/MLC upon GS[KD]. First, co-immunoprecipitation (co-IP) assays showed interac-

219   tion between endogenous RHOJ and GS (Fig. 5a). Such co-IP was not observed for RHOA

220   and RHOC (most abundant in ECs) (Extended Data Fig. 7a). Second, deletion of the first 20

221   N-terminal amino acids in RHOJ (ΔN20-RHOJ), mediating RHOJ's plasma membrane locali-

222   zation[19], reduced the interaction with GS (Extended data Fig. 7b). Third, immunoblotting

223   showed that only RHOJ, but not RHOA or RHOC, was predominantly membrane localized

224   (Extended data Fig. 7c). Fourth, we confirmed the GS-RHOJ interaction with a bimolecular

225   fluorescence complementation approach (BiFC) (Extended Data Fig. 7d,e). Based on the

226   above data, we focused on RHOJ as most likely interacting partner of GS.

227   To interact with membrane-localized (active) RHOJ, GS should be membrane localized

228   as well. Indeed, cell fractionation studies revealed that a fraction of GS was membrane local-

229   ized (Fig. 5b). Further evidence derives from single particle tracking data, acquired by photo-

230   activated localization microscopy imaging (SPT-PALM), combined with total internal reflection

231   fluorescence microscopy (TIRF). We traced the movement of single GS proteins tagged with

232   the photoswitchable fluorescent protein (PSFP) mEOS (GS-mEOS). Single GS-mEOS parti-

233   cles had a lower diffusion coefficient (DF) in the TIRF region (comprising the plasma mem-

234   brane and the immediately adjacent cytoplasm) than free mEOS, indicative of an association

235   of GS with membrane structures (Fig. 5c; Extended Data Fig. 7f).

236   PALMITOYLATION OF GS AND RHOJ

237   Membrane localization often requires post-translational palmitoylation. We thus hypothesized

238   that GS could be palmitoylated to allow plasma membrane localization and interaction with

239   RHOJ. Therefore, we performed click chemistry with biotin-azide (Extended Data Fig. 7g) on

240   lysates from HEK293 cells overexpressing GS and treated with the clickable palmitoylation

241   probes 16C-BYA or 16C-YA. Streptavidin pull-down showed clear palmitoylation of GS, as

242   both probes labeled GS. The labeling was reduced by MSO, consistent with the presumed

243   dependency of the phenotype on the enzyme's catalytic site (Fig. 5d).

244   GS was anecdotally reported previously to be palmitoylated, however without any fur-

245   ther in-depth molecular / functional characterization[20]. To determine if GS undergoes auto-

246   palmitoylation, we incubated purified GS[21] with palmitoyl-alkyne CoA (a substrate for pal-

247   mitoylation) in a cell-free system without any other proteins present, to demonstrate a direct

248   effect. Click chemistry revealed that increasing the dose of palmitoyl-alkyne CoA resulted in

249   increased autopalmitoylation of GS (Fig. 5e). Importantly, autopalmitoylation of GS was

250   achieved with physiological concentrations of palmitoyl-CoA (1-10 µM) at neutral pH, suggest-

251   ing physiologically relevant autopalmitoylation. An independent cell-free assay, relying on the

252   detection of CoA, released from palmitoyl-CoA during autopalmitoylation, confirmed these

253   findings (α-ketoglutarate dehydrogenase uses CoA to convert α-ketoglutarate + NAD$^+$ into

254   succinyl-CoA + NADH; NADH fluorescence is quantified) (Extended Data Fig. 7h-i). Further

255   confirmation was obtained using a cell-free affinity-chromatography-based binding assay with

256   palmitoyl-CoA immobilized on agarose beads. Recombinant GS was captured in a highly effi-

257   cient manner on these beads as evidenced by the relatively low levels of unbound protein in

258   the flow-through and the high protein amounts recovered in the SDS eluate (Extended Data

259   Fig. 7j).

260   Palmitoylation of target proteins by palmitoyl-acyl transferases (PATs) is a two-step re-

261   action, requiring first autopalmitoylation of the PAT, and thereafter, transfer of the palmitoyl

262   group to the target protein, though the precise molecular details of the latter step remain un-

263   clear (and could even occur non-enzymatically). We hypothesized GS to have a similar activi-

264   ty profile (Supplementary Discussion 2) and therefore explored if GS was involved in pal-

265   mitoylation of RHOJ. Even though RHOJ contains cysteine residues that are *in silico* predict-

266   ed to be high fidelity palmitoylation sites (screened with SwissPalm[22], data not shown), pal-

267   mitoylation of RHOJ has been poorly documented (except in a few studies[23,24]). Interestingly,

268   RHOJ's membrane localization and activity were reduced by treatment of ECs with the pan-

269   palmitoylation inhibitor 2-bromopalmitate (2BP) (Fig. 5f; Extended Data Fig. 7k-n), providing

270   initial evidence that RHOJ can be palmitoylated in ECs. Using the palmitoylation probe 17-

271   ODYA (Fig. 5g) or an acyl-resin-assisted capture (acyl-RAC; Extended Data Fig. 7o), we in-

272   deed found a reduction in the levels of palmitoylated RHOJ upon blocking GS, consistent with

273   a model whereby GS sustains palmitoylation of RHOJ.

274   ## DISCUSSION

275   Surprisingly, we found a glutamine synthesizing-independent activity for GS in regulating EC

276   motility, even though we cannot formally exclude a possible contribution of minimal levels of

277   glutamine production by GS to the observed phenotype. Indeed, GS regulates RHOJ signal-

278   ing in cell motility as shown by several lines of evidence. First, a fraction of GS is present in

279   EC membranes, where active RHOJ resides. Second, GS interacts with RHOJ in ECs in co-

280   IP experiments (though this interaction can be direct / indirect). Third, GS[KD] reduces RHOJ's

281   palmitoylation, membrane localization and activity in ECs. Thus, since RHOJ promotes EC

282   motility[13,17], the impaired migration of GS[KD] ECs could be attributed to the reduced RHOJ ac-

283   tivity.

284   However, RHOJ likely also indirectly contributes to promoting EC motility through con-

285   trolling the activity of the RHOA/ROCK/MLC signaling pathway, known to regulate EC motility

286   by affecting stress fiber formation[13,17]. Indeed, by lowering RHOJ's activity, *GS* silencing could

287   also indirectly increase RHOA/ROCK/MLC signaling, consistent with reports that RHOJ inhib-

288   its this pathway[13,17] (even though the precise molecular link between RHOJ and

289   RHOA/ROCK/ MLC signaling remains unknown, and a possible effect of GS[KD] on other small

290   GTPases or motility regulators cannot be excluded). Increased RHOA/ROCK/MLC signaling

291   would be expected to result in the accumulation of F-actin stress fibers and induction of a less

292   motile phenotype. Since a decrease in ROCK activity and myosin II contraction are necessary

293   to allow vessel branching[25], the increased stress fiber content, the impaired lamellipodia for-

294   mation and the reduced motility of GS^{KD} ECs can explain the observed *in vivo* vessel sprout-

295   ing defect (Extended Data Fig. 7p).

296   Because purified GS seems capable of autopalmitoylation (a trademark of PAT en-

297   zymes), and GS silencing lowers RHOJ palmitoylation, our data support a model, whereby

298   GS first autopalmitoylates itself and thereafter transfers the palmitoyl group to RHOJ, though

299   we cannot formally exclude that transfer of the palmitoyl group from GS to RHOJ occurs via

300   additional partners or even non-enzymatically. A possible model for GS palmitoylation is de-

301   scribed in Supplementary Discussion 3 and Extended Data Fig. 8. Also, whether the GS-

302   RHOJ partnership is exclusive or GS interacts with other players (*eg* other palmitoylated

303   RhoGTPases such as RAC1, CDC42, RHOU or RHOV) to mediate this effect on EC motility,

304   remains outstanding. In any case, RHOJ seems to be a critical target of GS, given that its si-

305   lencing completely phenocopies GS inhibition in ECs.

306   Finally, GS is critical for EC motility / migration, contributing to the formation of new

307   vessels in development and disease. In contrast, ECs do not migrate when they are quiescent

308   in healthy adults, explaining why GS inhibition has no observable effects on the vasculature in

309   healthy adult mice. This renders GS an attractive disease-restricted target for therapeutic in-

310   hibition of pathological angiogenesis. In agreement, the pharmacological GS blocker MSO

311   reduced pathological angiogenesis in blinding eye and psoriatic skin disease (Fig. 2), which

312   warrants further exploration of GS targeting in anti-angiogenesis.

313

314

315

316   **ONLINE CONTENT**

317   Methods and associated references, and Extended Data display items are available in the

318   online version of the paper.
319

ACKNOWLEDGMENTS

AUTHOR CONTRIBUTIONS

Study concept: PC; *experimental design*: GE, CD, ARC, JG and PC; *data acquisition*: GE, CD, ARC, JG, UB, MDR, GJ, JvR, GS, FC, AZ, SR, HH, SVa, JK, CL, FJMR, BC, LR, SVi, KB, SW, JS, LS, JHo, SL, RC, BG, MD, FLG, JvB, XW; *data analysis and interpretation*: GE, CD, ARC, JG, RC, UB, CL, SR, LT, BC, MD, JHo, SL, BG, FLG, JvB, XW and PC; *providing necessary materials*: WHL, YW and JHa; *manuscript drafting*: GE and PC; *critical revision*: all authors critically read the manuscript and had the opportunity to formulate remarks; all authors agreed on the final version of the manuscript; *scientific supervision*: PC.

CONFLICT OF INTEREST DECLARATION

The authors declare no conflict of interest.

AUTHOR INFORMATION

Reprints and permissions information is available at www.nature.com/reprints.

Correspondence and requests for materials should be addressed to PC (peter.carmeliet@ kuleuven.vib.be)

REFERENCES

1   De Bock, K. *et al.* Role of PFKFB3-Driven Glycolysis in Vessel Sprouting. *Cell* **154**, 651-663, doi:10.1016/j.cell.2013.06.037 (2013).

2   Schoors, S. *et al.* Fatty acid carbon is essential for dNTP synthesis in endothelial cells. *Nature* **520**, 192-197, doi:10.1038/nature14362 (2015).

3   Schoors, S. *et al.* Partial and transient reduction of glycolysis by PFKFB3 blockade reduces pathological angiogenesis. *Cell Metab* **19**, 37-48, doi:10.1016/j.cmet.2013.11.008 (2014).

4   Huang, H. *et al.* Role of glutamine and interlinked asparagine metabolism in vessel formation. *EMBO J* **36**, 2334-2352, doi:10.15252/embj.201695518 (2017).

5   Abcouwer, S. F., Lukascewicz, G. C., Ryan, U. S. & Souba, W. W. Molecular regulation of lung endothelial glutamine synthetase expression. *Surgery* **118**, 325-334; discussion 335 (1995).

6   He, Y., Hakvoort, T. B., Vermeulen, J. L., Lamers, W. H. & Van Roon, M. A. Glutamine synthetase is essential in early mouse embryogenesis. *Dev Dyn* **236**, 1865-1875, doi:10.1002/dvdy.21185 (2007).

7   Haberle, J. *et al.* Congenital glutamine deficiency with glutamine synthetase mutations. *N Engl J Med* **353**, 1926-1933, doi:10.1056/NEJMoa050456 (2005).

8   Kung, H. N., Marks, J. R. & Chi, J. T. Glutamine synthetase is a genetic determinant of cell type-specific glutamine independence in breast epithelia. *PLoS Genet* **7**, e1002229, doi:10.1371/journal.pgen.1002229 (2011).

9   Schoors, S. *et al.* Incomplete and transitory decrease of glycolysis: a new paradigm for anti-angiogenic therapy? *Cell Cycle* **13**, 16-22, doi:10.4161/cc.27519 (2014).

10   Dadsetan, S. *et al.* Brain alanine formation as an ammonia-scavenging pathway during hyperammonemia: effects of glutamine synthetase inhibition in rats and astrocyte-neuron co-cultures. *J Cereb Blood Flow Metab* **33**, 1235-1241, doi:10.1038/jcbfm.2013.73 (2013).

11   Ridley, A. J. Rho GTPase signalling in cell migration. *Curr Opin Cell Biol* **36**, 103-112, doi:10.1016/j.ceb.2015.08.005 (2015).

391 12 Yuan, L. *et al.* RhoJ is an endothelial cell-restricted Rho GTPase that mediates
392   vascular morphogenesis and is regulated by the transcription factor ERG. *Blood* **118**,
393   1145-1153, doi:10.1182/blood-2010-10-315275 (2011).

394 13 Kim, C. *et al.* Vascular RhoJ is an effective and selective target for tumor angiogenesis
395   and vascular disruption. *Cancer Cell* **25**, 102-117, doi:10.1016/j.ccr.2013.12.010
396   (2014).

397 14 Leszczynska, K., Kaur, S., Wilson, E., Bicknell, R. & Heath, V. L. The role of RhoJ in
398   endothelial cell biology and angiogenesis. *Biochem Soc Trans* **39**, 1606-1611,
399   doi:10.1042/BST20110702 (2011).

400 15 de Toledo, M. *et al.* The GTP/GDP cycling of rho GTPase TCL is an essential regulator
401   of the early endocytic pathway. *Mol Biol Cell* **14**, 4846-4856, doi:10.1091/mbc.E03-04-
402   0254 (2003).

403 16 Nethe, M. & Hordijk, P. L. The role of ubiquitylation and degradation in RhoGTPase
404   signalling. *J Cell Sci* **123**, 4011-4018, doi:10.1242/jcs.078360 (2010).

405 17 Kaur, S. *et al.* RhoJ/TCL regulates endothelial motility and tube formation and
406   modulates actomyosin contractility and focal adhesion numbers. *Arterioscler Thromb*
407   *Vasc Biol* **31**, 657-664, doi:10.1161/ATVBAHA.110.216341 (2011).

408 18 Heasman, S. J. & Ridley, A. J. Multiple roles for RhoA during T cell transendothelial
409   migration. *Small GTPases* **1**, 174-179, doi:10.4161/sgtp.1.3.14724 (2010).

410 19 Ackermann, K. L., Florke, R. R., Reyes, S. S., Tader, B. R. & Hamann, M. J. TCL/RhoJ
411   Plasma Membrane Localization and Nucleotide Exchange Is Coordinately Regulated
412   by Amino Acids within the N Terminus and a Distal Loop Region. *J Biol Chem* **291**,
413   23604-23617, doi:10.1074/jbc.M116.750026 (2016).

414 20 Wan, J. *et al.* Tracking brain palmitoylation change: predominance of glial change in a
415   mouse model of Huntington's disease. *Chem Biol* **20**, 1421-1434,
416   doi:10.1016/j.chembiol.2013.09.018 (2013).

417 21 Levine, R. L., Oliver, C. N., Fulks, R. M. & Stadtman, E. R. Turnover of bacterial
418   glutamine synthetase: oxidative inactivation precedes proteolysis. *Proc Natl Acad Sci*
419   *U S A* **78**, 2120-2124 (1981).

420 22 Blanc, M. *et al.* SwissPalm: Protein Palmitoylation database. *F1000Res* **4**, 261,
421   doi:10.12688/f1000research.6464.1 (2015).

422   23   Roberts, P. J. *et al.* Rho Family GTPase modification and dependence on CAAX motif-
423   signaled   posttranslational   modification.   *J   Biol   Chem*   **283**,   25150-25163,
424   doi:10.1074/jbc.M800882200 (2008).

425   24   Wei, X., Song, H. & Semenkovich, C. F. Insulin-regulated protein palmitoylation
426   impacts endothelial cell function. *Arterioscler Thromb Vasc Biol* **34**, 346-354,
427   doi:10.1161/ATVBAHA.113.302848 (2014).

428   25   Fischer, R. S., Gardel, M., Ma, X., Adelstein, R. S. & Waterman, C. M. Local cortical
429   tension by myosin II guides 3D endothelial cell branching. *Curr Biol* **19**, 260-265,
430   doi:10.1016/j.cub.2008.12.045 (2009).

431   26   Abraham, S. *et al.* VE-Cadherin-mediated cell-cell interaction suppresses sprouting via
432   signaling   to   MLC2   phosphorylation.   *Curr   Biol*   **19**,   668-674,
433   doi:10.1016/j.cub.2009.02.057 (2009).

434

435

436

437

438

439

440

441

442

443

444

445

446

447

448

LEGENDS TO FIGURES

FIGURE 1: EC-SPECIFIC DELETION OF GS CAUSES VASCULAR DEFECTS *IN VIVO*

a, GS expression (arrowheads) in the retinal microvasculature (co-stained with isolectin B4 (IB4)) of five day-old (P5) chimeric pups obtained by injection of $GS^{+/GFP}$ ES cells into wild type (WT) C57Bl/6 blastocysts (white boxed region is magnified in right panel). **b,** GS protein levels in primary human umbilical vein ECs under different extracellular glutamine levels (densitometric quantification of GS/ß-actin levels in % of 0 mM glutamine is shown on top). **c,** *GS* mRNA levels upon activation of VE-cadherin-Cre^{ERT2}. **d-g,** IB4 staining of P5 retinal vascular plexi from WT (d) and GS^{vECKO} (e) mice (pictures with zoom-in insets, A=artery, V=vein) and quantification of branch points at the front of the plexus (f) and radial expansion of the plexus (g). **h,** Vessel regression quantified as area of collagen IV (Col IV)$^+$ IB4$^-$ vessel sleeves (% of total Col IV$^+$ area) in retinas from P5 WT and GS^{vECKO} pups. **i-j,** Number of distal sprouts (i) and filopodia (j) per unit length of the retinal vascular front. **k-m,** Representative pictures for IB4 (gray)/EdU (cyan) double staining of P5 WT (l) and GS^{vECKO} (m) retinas (arrowheads in zoom-in insets denote EdU$^+$ ECs) and quantification (k) of EdU$^+$ ECs at the front of the plexus. **n-r,** CD31-stained dermal dorsal blood vasculature in E16.5 WT (n,o) and GS^{vECKO} (p,q) mice with boxed regions magnified in (o) and (q) and quantification of number of branch points per mm^2 (r). All data are mean±s.e.m; n=2 for densitometric quantification (b); n-numbers (individual mice) for WT and GS^{vECKO} are: 3 and 3 (c); 11 and 10 (f); 10 and 7 (g); 4 and 6 (h); 17 and 20 (i,j); 12 and 22 (k); 5 and 15 (r), from 2 (g,h,r), 3 (f) or 4 (i,j,k) litters. ^{NS}p>0.05, *p<0.05 according to Student's *t* test (c,g,h,i,k,r) or mixed models R statistics (f,j). Scale bars: 10 μm (a right), 50 μm (a left), 100 μm (l,m), 200 μm (d,e,n,p). For gel source images, see Extended Data Fig. 9.

472

473 **FIGURE 2:** GS INHIBITION MITIGATES PATHOLOGICAL ANGIOGENESIS

474 **a-d,** Retinal flat-mounts of retinopathy of prematurity (ROP) mice treated with vehicle (a) or 20

475 mg kg^{-1} d^{-1} MSO (b). Quantification of vascular tuft (c) and vaso-obliterated area (d) in control

476 and MSO-treated ROP pups. **e-g,** Quantification (e) of CD31^{+} (green) neo-vessels in corneal

477 flat-mounts from mice in corneal pocket assays (CPA) with bFGF pellets (demarcated by dot-

478 ted white line) additionally containing vehicle (f) or MSO (g). **h-l,** CD105 staining of untreated

479 skin (h), IMQ-treated skin (i), IMQ + low dose MSO-treated skin (j), IMQ + high dose MSO-

480 treated skin (k), and corresponding quantification of CD105^{+} area (l). All data are

481 mean±s.e.m.; n-numbers (individual mice) for control and MSO-treated are: 7 and 6 (c,d), 10

482 and 11 (e) from 3 litters (c,d) and 2 experiments (e). In (l) n=15 for control, n=22 for IMQ,

483 n=18 for IMQ + MSO (low; indicated by +) and n=6 animals for IMQ + MSO (high; indicated by

484 ++) from 3 experiments. ^{NS}p>0.05, *p<0.05 according to Student's *t* test (c,d,e) or ANOVA

485 with Dunnett's multiple comparisons *vs* IMQ (l). bFGF: basic fibroblast growth factor; CD31:

486 cluster of differentiation 31; IMQ: imiquimod; MSO: methionine sulfoximine. Scale bars: 100

487 μm (a,b), 200 μm (f,g), 75 μm (h-k).

488

489 **FIGURE 3:** LOSS OF *GS* IMPAIRS EC MIGRATION THROUGH PERTURBED ACTIN DYNAMICS

490 **a-f,** Control (a,c) and GS^{KD} (b,d) EC spheroids without (a,b) and with mitomycin C (MitoC)

491 (c,d) treatment and quantification of number of sprouts per spheroid (e) and total sprout

492 length (f). **g,** [^{3}H]-Thymidine incorporation into DNA in control and GS^{KD} ECs. **h,** Wound clo-

493 sure upon MitoC-treatment of control and GS^{KD} monolayers using the scratch assay. **i,**

494   Boyden chamber migration for control, GS^{KD} and GS^{KD} + rGS^{OE} (overexpression of a shRNA-

495   resistant *GS* mutant) ECs, all under MitoC-treatment. **j,** Velocity measurement using sparsely

496   seeded control and GS^{KD} ECs. **k-m,** Phalloidin (F-actin) staining of control (k) and GS^{KD} (l)

497   ECs (arrows and white dotted lines indicate lamellipodia) and quantification of lamellipodial

498   area (m). **n-p,** Quantification of F-actin/G-actin ratio in phalloidin (F-actin) – DNAse I (G-actin)

499   double-stained control and GS^{KD} ECs (n), and representative images of the phalloidin staining

500   of control (o) and GS^{KD} (p) ECs. **q-u,** Phalloidin staining of latrunculin B-treated control (q,s)

501   and GS^{KD} (r,t) ECs at timepoint 0 (q,r) and at 1 h after latrunculin wash-out (s,t) and quantifi-

502   cation of F-actin levels after wash-out (u). **v,** Quantification of α-tubulin levels in GS^{KD} and

503   control ECs. All data are mean±s.e.m.; n-numbers (independent experiments) are: 4 (e,f), 9

504   (g,j), 5 (h), 6 (i,u), 7 (m) and 3 (n,v). $^{NS}p>0.05$, $*p<0.05$ according to mixed models R statistics

505   (e,f), Student's *t* test (g,h,j,m,n,u,v) or ANOVA with Dunnett's multiple comparison *vs* control

506   (i). AU, arbitrary units. Scale bars: 100 µm (a-d), 10 µm (k,l) and 20 µm (o-t).

507

508   **FIGURE 4:** ENDOTHELIAL GS REGULATES RHOGTPASE ACTIVITY

509   **a,** Glutamine-producing activity at different extracellular glutamine levels measured as label

510   contribution of $^{15}NH_4^+$ to intracellular glutamine (% isotope enrichment in glutamine m+1 and

511   glutamate m+1 at 30 min after adding $^{15}NH_4^+$; MSO (1 mM) was used to block GS activity). **b,**

512   Immunoblots for RHOJ, NaK ATPase (NaK; membrane marker) and GAPDH (cytosol marker)

513   in cytosolic (c) and membrane (m) fractions with densitometric quantification **c,** Immunoblot

514   for active and total RHOJ with densitometric quantification (with inclusion of $RHOJ^{KD}$, beads

515   only and irrelevant biotinylated peptide as negative controls) **d,** Schematic diagram displaying

516   RHOJ's pivotal, though yet not fully understood (as highlighted by the question mark) role in

517 EC migration and stress fiber formation. **e-g,** Immunoblots for pull-down RHOA (e), RHOB (f)

518 and RHOC (g) activity assays with densitometric quantifications. **h,** Control and GS^{KD} ECs,

519 expressing the DORA RHOA biosensor, with quantification of whole-cell FRET startratio

520 (mean±s.e.m.; n=12 individual control ECs and n=9 GS^{KD} ECs). Look-up table (LUT) (color

521 bar) on the left denotes relative RHOA activities (ranging from blue=low to red=high). **i,** Ky-

522 mography analysis of DORA RHOA biosensor expressing ECs, showing abnormally short-

523 lived lamellipodia in GS^{KD} ECs and spatio-temporal deregulation of RHOA activity, with red

524 arrowheads indicating increased RHOA activity in the retracting lamellipodium of GS^{KD} ECs

525 (kymograph representative of 13 individual control and GS^{KD} cells analyzed). Look-up table

526 (LUT) (color bar) in the bottom left corner denotes relative RHOA activities (ranging from

527 blue=low to red=high). **j,** Immunoblots for ROCK1, ROCK2 and α-tubulin with densitometric

528 quantification. **k,** Immunoblots for pMLC, total MLC and α-tubulin (loading control) with densi-

529 tometric quantification. Both pMLC and total MLC levels were quantified densitometrically and

530 first corrected for their corresponding α-tubulin. Then the ratio of the corrected (c)

531 (c)pMLC/(c)MLC was calculated. **l,** Quantification of phalloidin-stained F-actin stress fibers

532 after latrunculin B wash-out in ECs pre-treated with the ROCK inhibitor Y27632. Values are

533 expressed relative to untreated non-silenced control (horizontal dotted line) **m-o,** Effect of

534 Y27632 pre-treatment on: spheroid sprouting defect in GS^{KD} spheroids (m), migration defect

535 of GS^{KD} ECs in scratch wound assay (n), and lamellipodial area (o). Values in n,o are ex-

536 pressed relative to untreated non-silenced control (horizontal dotted line). An effect of this in-

537 hibitor on baseline vessel formation has been documented previously[26]. pMLC: phosphory-

538 lated   myosin   light   chain;   Y27632:   (1R,4r)-4-((R)-1-aminoethyl)-N-(pyridin-4-

539 yl)cyclohexanecarboxamide, ROCK inhibitor. Scale bar is 25 µm in (h). All data are

540 mean±s.e.m.; n-numbers (independent experiments) are: 3 (a,e,f,m,n), 4 (c(MSO),h,k,l), 5 (o),

541   6 (b), 7 (j), 8 (c(GS^{KD}), g). ^{NS}p>0.05, *p<0.05; ANOVA with Dunnett's multiple comparisons *vs*

542   4 mM (a), one sample *t* test (b,c,e,f,g,j,k), Student's *t* test (h,l,n,o) or mixed models R statistics

543   (m). For gel source images, see Extended Data Fig. 9.

544

545   **FIGURE 5:** GS (AUTO)-PALMITOYLATION

546   **a,** Co-immunoprecipitation (Co-IP) of endogenous RHOJ and GS in ECs. Upper panel: im-

547   munoprecipitation (IP) of RHOJ, followed by immunoblotting (IB) for GS. Lower panel: IP for

548   GS, followed by IB for RHOJ. **b,** Immunoblot for GS and RHOJ in cytosolic (c) and membrane

549   (m) fractions in ECs with NaK ATPase (NaK) and GAPDH as membrane and cytoplasmic

550   fraction markers respectively. **c,** Quantification of the diffusion coefficient (DF, in μm^2 s^{-1}) of

551   single photoswitchable fluorescent protein mEOS and mEOS-fused GS (mEOS-GS) particles

552   in the plasma membrane region of ECs acquired by SPT-PALM under TIRF illumination (DFs

553   were calculated for 41 cells expressing mEOS and 37 expressing mEOS-GS) **d,** GS im-

554   munoblotting after streptavidin pull-down of biotin-azide clicked lysates from HEK-293T cells

555   (with or without GS overexpression and MSO treatment) for the indicated palmitoylation

556   probes. Input shows levels of GS overexpression. **e,** Dose-effect of palmitoyl-alkyne CoA on

557   autopalmitoylation of purified GS; biotin-azide clicking and subsequent HRP-streptavidin blot-

558   ting; input control on Coomassie-stained gel. **f,** Immunoblotting for RHOJ, NaK and GAPDH in

559   membrane (m) and cytosolic (c) fractions of control- and 2BP-treated ECs with densitometric

560   quantification. **g,** Palmitoylation of RHOJ in GS^{KD} and MSO-treated ECs. In gel fluorescence

561   for TAMRA-azide 17-ODYA (palmitoylation probe)-clicked FLAG-RHOJ is shown. FLAG de-

562   tection serves as loading control. 2BP, 2-bromopalmitate, pan-palmitoylation inhibitor. All data

563   are mean±s.e.m.; n-numbers (independent experiments) are: 3 (a,b,c,d,f,g), 2 (e). ^{NS}p>0.05,

*p<0.05; Student's *t* test (c); one sample *t* test (f,g). For gel source images, see Extended Data Fig. 9.

LEGENDS TO EXTENDED DATA FIGURES

EXTENDED DATA FIGURE 1: *GS* KNOCK-OUT IMPAIRS VESSEL SPROUTING

a, *GS* mRNA levels in human umbilical vein ECs (HUVEC; n=9 donors), lung ECs (n=5), colon ECs (n=4), liver ECs (n=3), human umbilical arterial ECs (HUAEC; n=2) and human blood outgrowth ECs (BOEC (n=2); (mean±s.e.m.; *p<0.05 *vs* HUVEC, Student's *t* test) and in HEPG2 cells (mean±s.e.m.; n=3; *p<0.05 *vs* HUVEC, Student's *t* test). **b-c,** Western blot of GS protein levels in HUVECs and HEPG2 cells in medium containing 0.6 mM glutamine (+) or 0.025 mM glutamine (-) (b), and in isolated mouse liver ECs (mLiECs) and mouse astrocytes (c) with α-tubulin as loading control (representative immunoblots of two independent experiments are shown). **d-e,** Genomic organization of the loxed *GS* allele before and after Cre-mediated excision (d) and correct recombination of the lox allele (L) in GS^{vECKO} and GS^{pECKO} mice upon tamoxifen (tam) treatment, as assessed by genomic DNA PCR (e; the PCR to amplify the loxed *GS* allele (lox) or to amplify the Cre-recombined allele (Δ) were run in separate reactions but loaded in the same lane). **f,** Quantification of branchpoints at the rear of the plexus in GS^{vECKO} mice (mean±s.e.m.; n=10 animals for GS^{vECKO} and 11 for wild-type (WT) controls from 3 litters; *p<0.05 *vs* WT littermates, mixed models R statistics). **g,** Pericyte coverage of retinal microvessels in WT and GS^{vECKO} littermates determined by NG2 staining and shown as NG2^{+} area as % of vessel area (mean±s.e.m.; n=4 animals for WT and 3 for

587   GS^{vECKO} from 1 litter; ^{NS}p>0.05 *vs* WT, Student's *t* test). **h,** Reduced complexity of the retinal

588   vascular front in P5 GS^{vECKO} *vs* WT animals determined by the number of branches on distal

589   sprouts (mean±s.e.m.; n=13 animals for WT and 21 for GS^{vECKO} from 5 litters; *p<0.05 *vs* WT,

590   Student's *t* test). **i,** Quantification of EdU$^+$ ECs at the rear of the plexus (mean±s.e.m.; n=12

591   animals for WT and 22 for GS^{vECKO} from 4 litters; ^{NS}p>0.05 *vs* WT littermates, Student's *t*

592   test). **j-m,** Isolectin B4 staining of P5 retinal vascular plexi from WT (j) and GS^{pECKO} (k) mice

593   (representative pictures with zoom-in insets, A=artery, V=vein) and quantification of branch

594   points at the front (l) and the rear (m) of the plexus (mean±s.e.m.; n=10 animals for WT and

595   18 for GS^{pECKO} from 4 litters; *p<0.05 *vs* WT littermates, Student's *t* test). **n-u,** Isolectin B4

596   staining of the retinal microvasculature of 3 week (P21)-old (n,o) and 6 week (P42)-old (r,s)

597   WT and GS^{vECKO} littermates (A=artery, V=vein). Lower left insets display higher magnification

598   of IB4-stained superficial plexus, whereas lower right insets display higher magnification of

599   the deep plexus. Also shown is the corresponding quantification of the vascular area (p,t) and

600   the branch point density (q,u) in the superficial and the deep layer (mean±s.e.m.; n=8 ani-

601   mals for WT and 8 for GS^{vECKO} at P21, from two litters; n=10 animals for WT and 14 for

602   GS^{vECKO} at P42, from four litters; ^{NS}p>0.05 *vs* WT, Student's *t* test). **v-ag,** Representative mi-

603   crographs of heart (v,z), liver (w,aa) and kidney (x,ab) sections from WT and GS^{vECKO} litter-

604   mates immunostained for the EC marker endoglin and of lung (y,ac) sections immunostained

605   for the EC marker CD34 and corresponding quantifications of endoglin$^+$ (ad, heart; ae, liver;

606   af, kidney) or CD34$^+$ (ag) vascular area (mean±s.e.m.; n=5 animals (4 for heart) for WT and 7

607   (6 for heart) for GS^{vECKO}, from two litters, ^{NS}p>0.05 *vs* WT, Student's *t* test). **ah-ai,** Repre-

608   sentative images of flat-mounted retinas from control (ah) and MSO-treated (ai) ROP mice

609   (vaso-obliterated area in white). Scale bars are 200 μm in j-k, n-o and r-s, 20 μm in v-ac and 1

610   mm in ah-ai. HEPG2: hepatocellular carcinoma cells; mLiEC: mouse liver ECs; Tam: tamoxi-

611   fen; lox: loxed allele; Δ: recombined allele; NG2: chondroitin sulfate proteoglycan 4; Edu: 5-

612   ethynyl-2'-deoxyuridine. For gel source images, see Extended Data Fig. 9.

613

614

615   **EXTENDED DATA FIGURE 2**: EFFECTS OF SILENCING AND PHARMACOLOGICAL INHIBITION OF

616   GS ON EC VIABILITY AND CENTRAL METABOLISM

617   **a,** *GS* mRNA levels in control ECs and ECs transduced with two different non-overlapping

618   shRNAs targeting *GS* (GS^{KD1} and GS^{KD2}; GS^{KD1} is used in the experiments in the main manu-

619   script and denoted as GS^{KD}) or transfected with scrambled siRNA (SCR) or siRNA targeting

620   *GS* (siGS). Data are expressed as % of the respective control, denoted by the horizontal dot-

621   ted line (mean±s.e.m.; n=28 independent experiments for GS^{KD1}, n=3 independent experi-

622   ments for GS^{KD2} and n=9 independent experiments for siGS; *$p<0.05$ *vs* the respective con-

623   trol; one sample *t* test). **b-c,** Quantification of number of sprouts (b) and total sprout length (c)

624   for spheroid sprouting assays with GS^{KD} ECs and GS^{KD} ECs expressing a shRNA-resistant

625   *GS* mutant (rGS^{OE}) (mean±s.e.m.; n=3 independent experiments; *$p<0.05$ and $^{NS}p>0.05$ *vs*

626   control; ANOVA with Dunnett's multiple comparison *vs* control). **d,** Viability of control and

627   GS^{KD} ECs as measured by lactate dehydrogenase (LDH) release assay (mean±s.e.m.; n=3

628   independent experiments; $^{NS}p>0.05$ *vs* control, Student's *t* test). **e,** Intracellular reactive oxy-

629   gen species (ROS) levels measured by CM-H$_2$DCFDA staining (mean±s.e.m.; n=3 independ-

630   ent experiments; $^{NS}p>0.05$ *vs* control, Student's *t* test). **f,** Energy charge measurement (([ATP]

631   + 1⁄2[ADP]) / ([ATP] + [ADP] + [AMP])) in GS^{KD} and control ECs (mean±s.e.m.; n=3 inde-

632   pendent experiments; $^{NS}p>0.05$ *vs* control, Student's *t* test). **g,** Ratio of oxidized glutathione

633   over total glutathione levels (GSSG/(GSH+GSSG)) in GS^{KD} and control ECs (mean±s.e.m.;

634 n=4 independent experiments; ^{NS}p>0.05 *vs* control, Student's *t* test). **h,** NADP/NADPH ratio in

635 GS^{KD} and control ECs (mean±s.e.m.; n=5 independent experiments; ^{NS}p>0.05 *vs* control, one

636 sample *t* test). **i-k,** Effect of GS^{KD} on major metabolic fluxes including glycolysis (i), glucose

637 oxidation (j) and glutamine oxidation (k) (mean±s.e.m.; n=3 independent experiments for (i),

638 n=5 for (j) and n=4 for (k); ^{NS}p>0.05 *vs* control, one sample *t* test). **l,m,** Oxygen consumption

639 rate (OCR) in control, MSO-treated and GS^{KD} ECs in basal state and after injection of oligo-

640 mycin, FCCP and antimycin A (l) (mean±s.e.m.; n=3 independent experiments), and calcula-

641 tion of OCR$_{BAS}$, OCR$_{ATP}$ and maximal respiration (m) (mean±s.e.m.; n=3 independent exper-

642 iments). AU: arbitrary units; CM-DCF: 5-(and-6)-chloromethyl-2′,7′-dichlorodihydrofluorescein

643 diacetate, acetyl ester; FCCP: carbonyl cyanide-4-(trifluoromethoxy) phenylhydrazone; OC-

644 R$_{BAS}$: basal oxygen consumption rate; OCR$_{ATP}$: ATP-generating oxygen consumption rate;

645 RFU: relative fluorescence units; MSO, methionine sulfoximine.

646

647 **EXTENDED DATA FIGURE 3:** *GS* KNOCK-DOWN REDUCES EC MOTILITY

648 **a,** Wound closure in control and GS^{KD2} EC monolayer scratch assays with or without MitoC-

649 pretreatment (mean±s.e.m.; n=7 and 5 independent experiments for with and without MitoC

650 respectively; *p<0.05 *vs* corresponding control; Student's *t* test). **b,** Quantification of lamel-

651 lipodial area (% of total cellular area) in control and GS^{KD2} ECs (mean±s.e.m.; n=3 independ-

652 ent experiments; *p<0.05 *vs* control; Student's *t* test). **c,** Wound closure in monolayer scratch

653 assays with SCR- and siGS-transfected ECs (mean±s.e.m.; n=5 independent experiments;

654 *p<0.05 *vs* SCR; Student's *t* test). **d,** Quantification of lamellipodial area (% of total cellular

655 area) in SCR- and siGS-transfected ECs (mean±s.e.m.; n=5 independent experiments;

656 *p<0.05 *vs* SCR; Student's *t* test). **e,** [^{3}H]-Thymidine incorporation into DNA in SCR- and

657 siGS-transfected ECs (mean±s.e.m.; n=3 independent experiments; [NS]p>0.05 *vs* SCR; Stu-

658 dent's *t* test).

659

660

661

662 **EXTENDED DATA FIGURE 4:** EFFECTS OF *GS* SILENCING ON CYTOSKELETON AND BARRIER

663 FUNCTION

664 **a-h,** Representative images of control (a,c,e,g) and GS[KD] (b,d,f,h) ECs after staining for α-

665 tubulin (a,b), F-actin (c,d) and nuclear staining (e,f). **i-k,** Representative images of phalloidin +

666 Hoechst-stained liver ECs 6 hours after isolation from control (i) and MSO-treated (j) mice,

667 and corresponding quantification of F-actin levels (k) (mean±s.e.m.; n=5 mice per group;

668 *p<0.05 *vs* control, Student's *t* test). **l-n,** Representative images of phalloidin-stained (F-actin)

669 confluent monolayer control (l) and GS[KD] (m) ECs aligning a scratch wound, and quantifica-

670 tion of F-actin levels (n) (mean±s.e.m.; n=5 independent experiments; *p<0.05 *vs* control,

671 Student's *t* test). **o,** Quantification of the length of discontinuous and continuous VE-cadherin-

672 stained junctions in control and GS[KD] ECs (mean±s.e.m.; n=4 independent experiments;

673 *p<0.05 *vs* control, Student's *t* test). **p,** Quantification of VE-cadherin gap size index in control

674 and GS[KD] EC monolayers (mean±s.e.m.; n=4 independent experiments; *p<0.05 *vs* control,

675 Student's *t* test). **q-v,** Corresponding representative images of monolayer control and GS[KD]

676 ECs stained for VE-cadherin (q,r,u,v) and F-actin (s,t,u,v). Yellow arrows in (r) point to discon-

677 tinuous VE-cadherin junctions and yellow asterisks indicate intracellular gaps. **w,** Quantifica-

678 tion of transendothelial electrical resistance (TEER) in control and GS[KD] EC monolayers

679 (mean±s.e.m.; n=4 independent experiments; *p<0.05 *vs* control, Student's *t* test at each time

point). **x-z,** Quantification (x) of Evans blue dye extracted from the ears of control and MSO-
treated mice induced by topical application of mustard oil (n=4 mice for each condition,
*p<0.05; Student's *t* test) and representative pictures of the Evans blue leakage into the ear
tissue in control (y) and MSO-treated (z) mice. Scale bar is 20 μm in a-h and in l-m and 10 μm
in i-j and in q-v. AU: arbitrary units.

EXTENDED DATA FIGURE 5: ENZYMATIC ACTIVITY OF GS AND ITS ROLE IN EC MIGRATION

a, Scheme of $^{15}NH_4^+$ labeling of glutamate and glutamine with blue circles representing unla-
beled carbons and red circles representing labeled nitrogen. **b,** ^{15}N incorporation into gluta-
mine (% isotope enrichment in m+1 and m+2 at 30 min after adding $^{15}NH_4^+$) in medium with
dialyzed serum and different levels of glutamine (mean±s.e.m.; n=3 independent experiments;
ANOVA with Dunnett's multiple comparisons *vs* 4 mM). **c,** ^{15}N incorporation into glutamate (%
isotope enrichment in m+1) and glutamine (% isotope enrichment in m+1 and m+2) at 30 min
after adding increasing concentrations of $^{15}NH_4Cl$ to the medium (mean±s.e.m.; n=3 inde-
pendent experiments). **d,** Scheme of ^{13}C labeling of glutamine from [U-^{13}C]-glutamate label-
ing, with blue circles representing unlabeled nitrogen and red circles representing labeled
carbons. **e,** Label contribution of [U-^{13}C]-glutamate to intracellular glutamine at various extra-
cellular glutamine levels (% isotope enrichment in glutamine m+5 and glutamate m+5 at 30
min after adding the tracer) (mean±s.e.m.; n=3 independent experiments; ANOVA with Dun-
nett's multiple comparisons *vs* 4 mM). **f,** Scheme representing contribution of [U-^{13}C]-glucose
carbons to glutamine with red circles representing labeled carbons and blue circles represent-
ing unlabeled carbons. Incorporation is shown after one turn of the TCA cycle only. **g,** Total
contribution of [U-^{13}C]-glucose carbons to α-ketoglutarate, glutamate and glutamine in ECs in

703   the presence or absence of glutamine in the medium at 48 h after adding the tracer

704   (mean±s.e.m.; n=3 independent experiments; *p<0.05 *vs* total contribution in gln at 0.6 mM

705   external gln, ANOVA with Dunnett's multiple comparisons). **h,** ^{15}N incorporation into gluta-

706   mine (% isotope enrichment in m+1 and m+2 at 30 min after adding ^{15}NH$_4^+$) in ECs and

707   HEPG2 cells (mean±s.e.m.; n=4 independent experiments (ND=not detected)). **i,** ^{13}C-

708   glutamine uptake kinetics in control, MSO-treated and GS^{KD} ECs and kinetics of subsequent

709   downstream conversion to glutamate. Data are expressed as m+5 isotopomer, as a percent-

710   age of the total intracellular pool of glutamine (gln) or glutamate (glu). The "0" timepoint is the

711   'theoretical' 0 when cells did not receive (and thus did not take up) any tracer; the "0.5 min"

712   timepoint represents uptake in cells, upon addition and immediate removal again of the tracer

713   (mean±s.e.m.; n=3 independent experiments; no statistical differences between control,

714   MSO-treated and GS^{KD} were observed at any of the individual time points for glutamine nor

715   for glutamate according to ANOVA with Dunnett's multiple comparison *vs* control at each time

716   point). **j,** Extracellular ^{14}C-glutamine uptake in control and GS^{KD} control ECs (mean±s.e.m.;

717   n=5 independent experiments; ^{NS}p>0.05 *vs* control, one sample *t* test). **k,** Ratio of intracellular

718   glutamine (gln) over glutamate (glu) levels in control and GS^{KD} ECs (mean±s.e.m.; n=3 inde-

719   pendent experiments; ^{NS}p>0.05 *vs* control, Student's *t* test). **l,** Velocity measurement of con-

720   trol and GS^{KD} ECs at different concentrations of glutamine (gln) in the medium (mean±s.e.m.;

721   n=4 independent experiments; *p<0.05 *vs* corresponding control, mixed models R statistics).

722   **m-n,** Effect of increased concentrations of external glutamine on the number of sprouts (m)

723   and total sprout length (n) in control and GS^{KD} spheroids (mean±s.e.m.; n=3 independent ex-

724   periments; *p<0.05 *vs* corresponding control, mixed models R statistics). **o-p,** Quantification

725   of number of sprouts per spheroid (o) and total sprout length (p) in control and MSO-treated

726   EC spheroids (mean ± s.e.m.; n=3 independent experiments; *p<0.05 *vs* control, Student's *t*

test). **q-s,** Effect of MSO-treatment on EC motility parameters: wound closure of MitoC-

treated ECs (q) (mean±s.e.m.; n=11 independent experiments; *p<0.05 *vs* control, Student's *t*

test), lamellipodial area (r) (mean±s.e.m.; n=10 independent experiments; *p<0.05 *vs* control,

Student's *t* test) and F-actin levels at 1 hour after latrunculin wash-out (s) (mean±s.e.m.; n=4

independent experiments; *p<0.05 *vs* control, one-sample *t* test). **t,** [^{3}H]-Thymidine incorpora-

tion into DNA in control and MSO-treated ECs (mean±s.e.m.; n=3 independent experiments;

^{NS}p>0.05 *vs* control, Student's *t* test). α-keto: α-ketoglutarate; GDH: glutamate dehydrogen-

ase; glu: glutamate; GS: glutamine synthetase; gln: glutamine; MSO, methionine sulfoximine;

MitoC: mitomycin C.

EXTENDED DATA FIGURE 6: RESCUING THE GS^{KD} PHENOTYPE *IN VITRO*

a, Schematic representation of the DORA RHOA FRET biosensor, depicting from N- to C-

terminal the circular permutated RHOA effector protein kinase N (cpPKN), the dimeric circular

permutated Venus (dcpVen), the ribosomal protein-based linkers (L9), the dimeric Cerulean3

(dCer3) and RHOA. **b-m,** Representative images of control (b-d), MSO-treated (e-f), GS^{KD} (h-

j) and RHOJ^{KD} (k-m) ECs after staining for F-actin (phalloidin) (c,e,f,h,i,k,l,n) and pMLC

(d,e,g,h,j,k,m,n). **n,** Quantification of the pMLC-immunoreactivity (mean±s.e.m.; n=6 inde-

pendent experiments; *p<0.05 *vs* control, one sample *t* test). **o-t,** Representative images of

control (o,q,s) and GS^{KD} (p,r,t) EC spheroids treated with vehicle (o,p) or the ROCK inhibitors

Y27632 (q,r) or fasudil hydrochloride (s,t). **u-v,** Quantification of the number of sprouts per

spheroid (u) and sprout length (v) (mean±s.e.m.; n=3 independent experiments; *p<0.05 and

^{NS}p>0.05 *vs* untreated control, ANOVA with Dunnett's multiple comparisons *vs* untreated con-

trol). **w,** Quantification of the lamellipodial area in vehicle- or fasudil hydrochloride-treated

750   control and GS^{KD} ECs (mean±s.e.m.; n=6 independent experiments; *p<0.05 and ^{NS}p>0.05 *vs*

751   untreated control, ANOVA with Dunnett's multiple comparisons *vs* untreated control). **x,**

752   Quantification of the lamellipodial area in vehicle-, ML7- or peptide 18-treated GS^{KD} and con-

753   trol ECs (mean±s.e.m.; n=4 independent experiments of which 3 experiments included the

754   ML7-treatment; *p<0.05 *vs* untreated control, ANOVA with Dunnett's multiple comparisons *vs*

755   untreated control). **y,** Scratch wound closure in vehicle-, ML7- or peptide 18-treated GS^{KD} and

756   control ECs (mean±s.e.m.; n=3 independent experiments; *p<0.05 *vs* untreated control,

757   ANOVA with Dunnett's multiple comparisons *vs* untreated control). **z,** Fold-changes (*vs* un-

758   treated control ECs) in F-actin levels from phalloidin-stained vehicle-, ML7- or peptide 18-

759   treated GS^{KD} ECs (mean±s.e.m.; n=4 independent experiments of which 3 included the pep-

760   tide 18-treatment; *p<0.05 *vs* untreated control, one sample *t* test). **aa,** Fold-changes (*vs* un-

761   treated control ECs) in pMLC levels from pMLC-immunostained vehicle-, ML7- or peptide 18-

762   treated GS^{KD} ECs (mean±s.e.m.; n=4 independent experiments of which 3 included the pep-

763   tide 18-treatment; *p<0.05 *vs* untreated control, one sample *t* test. Fasu., fasudil hydrochlo-

764   ride; pep 18, peptide 18. Scale bar is 20 μm in (b-m) and 100 μm in (o-t). For gel source im-

765   ages, see Extended Data Fig. 9.

766

767   **EXTENDED DATA FIGURE 7:** RHOGTPASE LOCALIZATION AND INTERACTION WITH GS

768   **a,** Co-immunoprecipitation (Co-IP) assays showing no detectable interaction between GS and

769   RHOA or RHOC (red asterisk indicates a non-specific band, which is present to the same ex-

770   tent in the IgG controls and which is not affected by shRNA mediated knock-down of either

771   RHOA or RHOC; no band at the correct height (see input) was detected). Picture shown is

772   representative for 3 independent experiments. **b,** Co-IP of overexpressed GS and RHOJ-

773   EGFP or ∆N-RHOJ-EGFP in ECs. Densitometric quantifications of immunoblotted (IB) bands

774   are mean±s.e.m.; n=4 independent experiments; *p<0.05, one-sample *t* test *vs* GS – RHOJ-

775   EGFP Co-IP. In some of the experiments, the expression of the ∆N20-RHOJ-EGFP was low-

776   er than the expression of RHOJ-EGFP. To correct for this possible bias, densitometric quanti-

777   fication of all bands was performed in ImageJ and signals in the IP lanes were normalized to

778   the input signals. **c,** Immunoblotting for RHOA and RHOC on cytosolic (c) and membrane (m)

779   fractions of ECs. Na/K ATPase (NaK) was used as a membrane marker, GAPDH was used

780   as cytosolic marker. Picture shown is representative for 3 independent experiments. **d,**

781   Schematic representation of the bimolecular fluorescence complementation (BiFC) assay with

782   GS coupled to the N-terminal half of EGFP, and RHOJ coupled to the C-terminal half of

783   EGFP. Only when GS and RHOJ are in close proximity, the two EGFP half-sites complement

784   each other and form a functional EGFP. **e,** Fold-increase in the ratio of HEK cells showing de-

785   tectable EGFP complementation versus cells showing no detectable EGFP complementation;

786   a construct overexpressing an unfused N-terminal EGFP half-site together with RHOJ cou-

787   pled to the C-terminal EGFP half-site was used as a negative control (mean±s.e.m.; n=4 in-

788   dependent experiments; *p<0.05 *vs* control, Student's *t* test). **f,** Schematic representation of

789   SPT-PALM imaging under TIRF illumination with the plasma membrane lipid bilayer depicted

790   at the top. The TIRF region is shown in bright colors whereas the part of the cell outside of the

791   TIRF region in grayed out; the TIRF region contains the plasma membrane and its immediate-

792   ly adjacent space, which for the reasons of clearly depicting the principle of this assay are not

793   shown at their exact relative dimensions. Weight (boldness) and number of arrowheads rep-

794   resent velocity of single particles being either the photoswitchable fluorescent protein (PSFP)

795   or the PSFP coupled to the protein of interest (GS in this study). The PSFP is activated upon

796   entry into the TIRF region and is therefore color-coded differently inside *vs* outside of the

797   TIRF region. PSFP-GS displays reduced velocity in the TIRF region, presumably because of

798   palmitoylation and subsequent membrane association of GS. **g,** Schematic representation of

799   in-cell labeling of proteins with clickable alkyne-containing palmitoylation probes and subse-

800   quent biotin-azide clicking. X represents a possible palmitoylated protein, N_3 is the azide

801   group coupled to biotin. **h-i,** Rate of CoA release from palmitoyl-CoA as readout for recombi-

802   nant human GS autopalmitoylation while varying either the doses of palmitoyl-CoA (h) or the

803   amounts of recombinant GS (i) (mean±s.e.m.; n=4 independent experiments for h and n=5 for

804   i; *p<0.05, ANOVA with Dunnett's multiple comparisons *vs* 0 µM palmitoyl-CoA or *vs* 0.5 µg

805   recombinant GS). **j,** Representative GS immunoblot (of 3 independent experiments) for bind-

806   ing of recombinant human GS to palmitoyl-CoA agarose. IF=input fraction; FT=flow through;

807   W8=wash fraction 8; SDS=eluate. **k-m,** Effect of treatment with the pan-palmitoylation inhibi-

808   tor 2BP on RHOJ localization in ECs. Representative images of RHOJ-EGFP overexpressing

809   ECs under vehicle-treatment (k) or 2BP-treatment (l). Red arrowheads indicate EGFP signal

810   at membrane ruffles, which was quantified as percent of total cellular area (m) (mean±s.e.m.;

811   n=4 independent experiments; *p<0.05 *vs* vehicle-treated, Student's *t* test). **n,** RHOJ activity

812   (CRIB pull-down) in ECs under vehicle- or 2BP-treatment (blots shown are representative of 3

813   independent experiments; densitometric quantification in arbitrary units (AU) is mean±s.e.m;

814   *p<0.05, paired Student's *t* test *vs* vehicle-treated). **o,** Representative RHOJ immunoblotting

815   for control and GS^{KD} ECs overexpressing RHOJ ($RHOJ^{OE}$) subjected to acyl-RAC. The

816   cleaved bound fraction (cBF) represents the fraction with palmitoylated RHOJ. IF is the input

817   fraction, whereas the cleaved unbound fraction (cUF) and the preserved bound fraction (pBF)

818   are control fractions showing efficient depletion of RHOJ from the thioester cleaving reagent

819   and near absence of non-specific binding of RHOJ to the resin, respectively (for further detail

820   see Methods section). Densitometric quantification of cBF/IF is shown (mean±s.e.m; n=3 in-

821   dependent experiments; *p<0.05, one-sample *t* test *vs* control). **p,** GRAPHICAL ABSTRACT: *Left*

822   *side:* Autopalmitoylation allows endothelial GS to interact directly (or indirectly) with the

823   RhoGTPase RHOJ and to sustain RHOJ's palmitoylation, membrane localization and activity

824   (reflected by GTP binding). RHOJ activity then sustains normal EC migration and lamellipodia

825   formation, and keeps actin stress fiber formation at levels, promoting normal EC migration

826   and vessel branching *in vivo*. Through mechanisms that are incompletely understood at pre-

827   sent (indicated by the question mark), active RHOJ inhibits signaling of the RHOA/B/C –

828   ROCK – (p)MLC pathway (itself known to promote stress fiber formation and to reduce EC

829   motility). The relative contribution of a direct effect of RHOJ on migration *vs* the indirect effect

830   through RHOA/B/C – ROCK – (p)MLC remains to be determined.   Reduced opacity of

831   RHOA/B/C, ROCK and (p)MLC indicates reduced signaling of this pathway. GTP: guanosine

832   triphosphate. *Right side*: Loss of endothelial GS renders RHOJ less active (visually reflected

833   by fewer palmitoylated, membrane-bound RHOJ proteins), and weakens the brake on the

834   RHOA/B/C – ROCK – (p)MLC pathway. The resulting excessive stress fiber formation causes

835   ECs to lose migratory capacity and reduces vessel branching *in vivo*. Dashed lines indicate

836   reduced activity; red X indicates GS blockade; the question mark indicates unknown mecha-

837   nisms. Scale bar is 200 μm in k-l. For gel source images, see Extended Data Fig. 9.

838

839   **E**XTENDED **D**ATA **F**IGURE **8:** POSSIBLE MOLECULAR MODEL OF GS AUTOPALMITOYLATION

840   **a.** Structure of human GS and of its bifunnel-shaped catalytic site. Schematic representation

841   of the GS decamer in top and front view with individual subunits A and B labeled and colored

842   gray and green, respectively. Close-up of the bifunnel catalytic site which is formed between

843   subunits A and B. The GS decamer has 10 active sites, each located at the interface of two

844   adjacent subunits. ATP enters from the top whereas glutamate enters from below; Manga-

845   nese ions (Mn^{2+}) are shown as metalic spheres. **b.** Molecular dynamics (MD) simulation of

846   palmitoyl-CoA in the catalytic cleft of GS predicts that, while the head of palmitoyl-CoA is

847   tightly bound to the adenine binding site, the tail can point in opposing directions with respect

848   to the protein's principal axis. The most representative structures of the two alternative poses

849   observed during the long MD simulations for palmitoyl-CoA binding to GS (in blue, seen from

850   two different perspectives) are shown in red (A, tail bending upwards) and green (B, tail bend-

851   ing downwards). **c.** Detailed view on the main conformation – conformation A – is shown in

852   more details. The sulfur atom of palmitoyl-CoA (which is immediately adjacent to the carbon

853   on which the nucleophilic attack occurs) (colored yellow) approaches the highly conserved

854   C209 (also colored yellow), with an interatomic distance (S-S) that during the simulations re-

855   versibly fluctuates between 3 and 8 Å. The hydrophobic tail positions itself along grooves

856   characterized by the presence of hydrophobic residues. Color coding: carbons are grey, ni-

857   trogens blue, phosphorous golden and oxygens red. Cysteines and serines within 5 Å from

858   the palmitoyl tail are highlighted in yellow and orange, respectively. The hydrophobic residues

859   around the tail are shown in green. **d.** Detailed view on conformation B where the tail is found

860   in a buried hydrophobic cleft, with the sulfur at a distance of 5 Å or less from the conserved

861   serines 65 and 75 and the tail occupying the site of the GS inhibitor MSO. Details are shown

862   of the extensive steric clash between MSO and the secondary binding pose (B) observed in

863   palmitoyl-CoA MD simulations. Palmitoyl-CoA is represented as sticks with standard atomic

864   colours. MSO is shown in cyan and its position is taken from the 2QC8 entry in the protein

865   databank. Cysteines and serines within 5 Å from the palmitoyl tail are highlighted in yellow

866   and orange, respectively. The hydrophobic residues around the tail are shown in green. **e.** GS

867   immunoblotting after streptavidin pull-down of biotin-azide clicked lysates from 16C-YA (pal-

868   mitoylation probe) labeled HEK-293T cells overexpressing wild type *GS* or *GS* point-mutated

869   for C209. The input shows the level of GS overexpression. Representative blot for 4 inde-

870   pendent experiments is shown. **f-g.** Quantification of total sprout length (f) and number of

871   sprouts per spheroid (g) for control and GS^{KD} ECs with or without overexpression of shRNA

872   resistant C209A-point mutated *GS* (rGS$^{C209A-OE}$) (mean ± s.e.m.; n=4 independent experi-

873   ments; *p<0.01 *vs* control, ANOVA with Dunnett's multiple comparison *vs* control). **h.** Sche-

874   matic representation of protein autopalmitoylation. Upon binding of palmitoyl-CoA to the pro-

875   tein, free CoA (gray oval) is released and can be detected. **i.** Recombinant wild-type (WT) and

876   point-mutated (R324C and R341C) GS were incubated with different doses of palmitoyl-CoA

877   in a cell-free system at physiologcial pH. Release of CoA per minute was determined as a di-

878   rect readout for protein autopalmitoylation. **j.** Different amounts of recombinant WT, R324C

879   and R341C GS were incubated with a fixed amount of palmitoyl-CoA (40 µM) and CoA re-

880   lease per minute was determined as readout for autopalmitoylation. Data are mean ± s.e.m.

881   of at least 3 independent experiments. ^{NS}p>0.05; *p<0.05 according to two way ANOVA com-

882   paring the entire dose-response to the dose-response of WT GS. The data for WT GS from

883   panels (i) and (j) are also included in Extended Data Fig. 7 as stand-alone data, but are in-

884   cluded here too for comparison purposes. **k.** Boyden chamber migration for control, GS^{KD},

885   GS^{KD} + rGS^{OE} (r = shRNA-resistant; OE = overexpression), GS^{KD} + rGS$^{R341C-OE}$ and GS^{KD} +

886   rGS$^{R324C-OE}$ ECs, all under mitomycin C-treatment (mean ± s.e.m.; n=3 independent experi-

887   ments; ^{NS}p>0.05; *p<0.05, ANOVA with Dunnett's multiple comparison *vs* control). For gel

888   source images, see Extended Data Fig. 9.

889

890   **EXTENDED DATA FIGURE 9:** UNCROPPED GEL PICTURES AND BLOTS WITH SIZE MARKERS

891

892

893

894

895

896 ## METHODS

897 **CHEMICALS AND REAGENTS:** The GS inhibitor L-methionine sulfoximine (MSO), mitomycin C,

898 latrunculin B, oligomycin, antimycin A, carbonyl cyanide-4-(trifluoromethoxy) phenylhydrazone

899 (FCCP), 2-bromohexadecanoic acid (2-bromopalmitic acid, 2BP), tamoxifen, palmitoyl-CoA

900 agarose and α-ketoglutarate dehydrogenase were from Sigma-Aldrich. 17-Octadecynoic acid

901 (17-ODYA) was purchased from Cayman Chemical. The use and/or synthesis of the other

902 palmitoylation probes 15-hexadecynoic acid (16C-YA; a palmitate-based probe that binds a

903 broader spectrum of proteins than 16C-BYA (here below), including both PATs and PAT tar-

904 get proteins) and 2-bromooctadec-15-yonic acid (16C-BYA; a 2-bromopalmitate-based activi-

905 ty-based probe that labels but also inhibits palmitoyl acyltransferase (PAT) enzymes) has

906 been described previously[27]. The ROCK kinase inhibitor Y27632 was from BioVision, fasudil

907 hydrochloride and H1152 dihydrochloride are from Tocris. The MLCK inhibitors ML7-

908 hydrochloride and peptide 18 were from Tocris. Collagen type 1 (rat tail) was obtained from

909 Merck Millipore. [5-^{3}H]-glucose, [^{3}H]-thymidine, [U-^{14}C]-glutamine were from Perkin Elmer; [6-

910 ^{14}C]-D-glucose was from ARC. [U-^{13}C]-glucose, [U-^{13}C]-glutamine, [U-^{13}C]-glutamate and

911 ^{15}NH$_4$Cl were purchased from Cambridge Isotope Laboratories. The following primary anti-

912 bodies or dyes were used: *Griffonia simplicifolia* (GS)-IB$_4$-Alexa 488, isolectin GS-IB$_4$-Alexa

913 568, isolectin GS-IB$_4$-Alexa 647, phalloidin-Alexa 488, deoxyribonuclease I-Alexa 594 (Mo-

914   lecular Probes), anti-collagen IV (2150-1470) (Bio Rad), anti-GS (MAB302) and anti-NG2

915   Chondroitin Sulfate Proteoglycan (AB5320) (Millipore), anti-FLAG (clone M2), anti-GS (clone

916   2B12), anti-RHOJ (clone 1E4), anti-ROCK1 (HPA007567), anti-α-tubulin (T6199) (Sigma-

917   Aldrich), anti-β-actin (13E5), anti-phospho-Myosin Light Chain 2 and anti-Myosin Light Chain

918   2 (9776), anti-Na,K-ATPase (3010), anti-RHOA (67B9) and anti-RHOC (D40E4) (Cell Signal-

919   ing Technology), anti-CD105/endoglin (AF1320), anti-VE-cadherin (AF1002) (R&D Systems),

920   anti-GS (ab176562) (Abcam), anti-ROCK2 (A300-047A-T) (Imtec Diagnostics), anti-CD31

921   (MEC13.3), anti-CD34-biotin (#553732) (BD Biosciences). Secondary Alexa-405, -488, -568

922   or -647 conjugated antibodies were from Molecular Probes; other secondary antibodies and

923   IgG controls were from Dako. The Click-iT® 5-ethynyl-2´-deoxyuridine (EdU) Alexa Fluor® 555

924   Imaging Kit was from Invitrogen. Purified bacterial GS was a kind gift from Rod Levine (Be-

925   thesda, MD, USA).

926   **CELL CULTURE:** *HUMAN UMBILICAL VEIN ENDOTHELIAL CELLS (HUVECS) AND HUMAN UMBILICAL AR-*

927   *TERY ENDOTHELIAL CELLS (HUAECS)* obtained under protocol S57123 (Commission Medical

928   Ethics of UZ/KU Leuven) after written consent of the donors, were isolated as previously de-

929   scribed [1,2] and were routinely cultured in M199 medium (Invitrogen) containing 20% FBS, 0.6

930   mM L-glutamine, heparin (10U ml^{-1}; Sigma)), penicillin (100U ml^{-1}), streptomycin (100μg ml^{-1})

931   and endothelial cell growth factor supplements (EGCS; 30 mg l^{-1}; Sigma). Cells were only

932   used between passages 1 and 4 and all experiments were performed in HUVECs from at

933   least three different donors unless stated otherwise. Also except when stated otherwise, the

934   use of the abbreviation EC in the text refers to HUVEC. *ISOLATION OF ENDOTHELIAL CELLS FROM*

935   *HUMAN LUNG/LIVER/COLON MUCOSA*: Lung/liver/colon mucosa specimens were obtained under

936   protocol S57123 (Commission Medical Ethics of UZ/KU Leuven) and were washed several

937   times with phosphate buffer solution (PBS) and minced with scissors prior to enzymatic diges-

938   tion for 45 min. at 37 °C with collagenase/dispase/DNase solution (Gibco, Life Technologies).

939   The resulting suspension was passed through a 100 μm nylon mesh (BD Biosciences

940   Pharmingen) to remove aggregates. The harvested cells were washed, seeded on gelatine

941   pre-coated 6-well plates and cultured in complete endothelial growth medium (EGM-MV; Lon-

942   za) supplemented with antibiotics. After 5-7 days, when cells reached confluency, a positive

943   CD31 magnetic bead selection was performed (CD31 MicroBead, #130-091-935, Miltenyi Bio-

944   tech) according to the manufacturer's guidelines and purified cells were further cultured in

945   EGM medium. *PERIPHERAL BLOOD OUTGROWTH ENDOTHELIAL CELLS (BOECS)* were established

946   and cultured as previously described [28]. In brief, blood samples (obtained under protocol

947   S57123 (Commission Medical Ethics of UZ/KU Leuven) were diluted with PBS prior to Ficoll

948   PaquePLUS (GE Healthcare) density-gradient centrifugation at 1,000 g for 20 min at room

949   temperature. The mono-nuclear cell layer was collected, washed with PBS and resuspended

950   in EGM2 medium (PromoCell). Cells were plated in collagen-coated flasks and medium was

951   replaced every 2 days. From day 7 onwards, cells were checked for the formation of colonies,

952   which were allowed to grow up to approximately 1 cm^2. BOEC colonies were then trypsinized

953   and subcultured. *HEK293A AND HEPG2* CELLS (ATCC) were grown in DMEM, supplemented

954   with 10% fetal bovine serum (FBS), 100 U ml^{-1} penicillin and 100 μg ml^{-1} streptomycin. When

955   HEPG2 cells were compared directly to ECs in short term stable isotope tracing experiments,

956   they were incubated in exactly the same medium as the ECs to rule out possible bias coming

957   from the difference in media formulation. *MOUSE LIVER ENDOTHELIAL CELLS (MLIECS)* were iso-

958   lated from perfused healthy livers of control or GS^{ECKO} mice. Prior to perfusion, the mice were

959   anesthetized with Nembutal (60 mg kg^{-1}). Mice were perfused with 5 ml of a water based per-

960   fusion buffer containing 1.7 M NaCl, 84 mM KCl, 120 mM HEPES and 1 mM NaOH followed

961   by 5 ml of a PBS-based digestion buffer containing 0.1% collagenase II (Life Technologies),

962   collagenase I (Life Technologies), 2 mM CaCl$_2$, 1% antibiotic-antimycotic (Life Technologies)

963   and 10% FBS (Biochrome, Berlin, Germany) at a perfusion rate of 1 ml min^{-1}. Perfusion was

964   considered complete when the liver and mesenteric vessels were blanched and the desired

965   amount of digestion buffer (≥ 5ml) had passed through the circulatory system. Livers were

966   dissected, placed into a 50 ml conical tube with 3 ml of digestion buffer and incubated at 37

967   °C for approximately 30 min, with regular shaking of the tubes every 5 min. After digestion,

968   the tissue was homogeneously dissociated and the reaction was stopped with 10 ml of isola-

969   tion buffer containing PBS + 0.1% BSA (Sigma-Aldrich). Subsequently, the cell suspension

970   was filtered through a 100 μm cell strainer and cells were washed twice with isolation buffer.

971   Finally, the ECs were isolated by magnetic bead sorting with Dynabeads (CELLection^{TM} Biotin

972   Binder Kit, Life Technologies, Ghent, Belgium) coated with anti-mouse CD31 (eBioscience,

973   Anti-Mouse CD31 Clone 390), according to the manufacturer's instructions. Briefly, the cell

974   suspension was incubated with the beads at room temperature for 30 min in HulaMixer®

975   Sample Mixer (Life Technologies, Ghent, Belgium). Next, CD31^{+} ECs were collected by put-

976   ting the tubes on a DynaMag^{TM}-50 Magnet (Life Technologies) and removing the supernatant.

977   The procedure was repeated twice to remove cells debris. Finally, cells were resuspended in

978   EGM2 medium (PromoCell) and plated at the desired density on cell culture plates pre-coated

979   with 0.1% gelatin, and grown to confluency. MOUSE ASTROCYTES were prepared as described

980   previously with minor changes [29]. Briefly, spinal cords were dissected from 13-day old

981   C57BL/6J mouse embryos. Meninges and dorsal root ganglia were removed and a single cell

982   population was obtained by digestion with 0.05% trypsin in combination with gentle trituration.

983   The cell suspension was layered on a 6.2% OptiPrep™ (Axis-Shield, Oslo, Norway) cushion

984   and centrifuged at 500g for 15 min. The pellet was resuspended and the cells were plated

985   (12,000 cells cm^{-2}) in L15 medium supplemented with glucose (3.6 mg ml^{-1}), sodium bicar-

986 bonate (0.2%), penicillin 100 IU ml^{-1}), streptomycin (100 μg ml^{-1}) and fetal bovine serum

987 (10%). After reaching confluency, cell division was halted by treatment with cytosine arabino-

988 side (10 μM, 3 days). After 4 weeks, more than 95% of cells stained positive for glial fibrillary

989 acidic protein (GFAP; not shown).

990 **PLASMID CONSTRUCTIONS AND LENTIVIRAL PARTICLE PRODUCTION:** cDNA for human *GS* was ob-

991 tained from Origene. Silent mutations were introduced to make the *GS* cDNA resistant to the

992 *GS*-specific shRNA (see below, TRCN0000045628). Point-mutated constructs were generat-

993 ed with Stratagene's QuickChange site-directed mutagenesis kit following manufacturer's

994 guidelines. The cDNA for *RHOJ-EGFP* (*GFP-TCL*) was a gift from Channing Der (Addgene

995 plasmid # 23231) [23] and was used as a template to generate the N-terminal truncated ΔN20-

996 RHOJ-EGFP, lacking the first 20 amino acids and FLAG-tagged RHOJ. Standard cloning

997 techniques were used to fuse GS to the photoswitchable fluorescent protein mEOS (pRSETa-

998 mEos2 was a gift from Loren Looger; Addgene plasmid # 20341)[30]. The BiFC vector allowing

999 simultaneous expression of two separate cDNAs fused to EGFP subfragment 1 (N-terminal;

1000 containing amino acids 1 to 158) or subfragment 2 (C-terminal; containing amino acids from

1001 159 onwards) respectively was a kind gift of Prof. Hideaki Mizuno (KU Leuven). GS was fused

1002 to the N-terminal subfragment of EGFP and RHOJ was fused to the C-terminal EGFP sub-

1003 fragment to generate GS-EGFP$^{1/2}$, RHOJ-EGFP$^{2/2}$. Lentiviral expression constructs were ob-

1004 tained by cloning the respective cDNAs into pRRLsinPPT.CMV.MCS MM WPRE-vector. Vali-

1005 dated *GS*-specific (TRC clones TRCN0000045628 (used in the majority of the experiments

1006 and indicated as GS^{KD1} in Extended Data Fig. 2a) and TRCN0000045631 (indicated as GS^{KD2}

1007 in Extended Data Fig. 2a and only used to confirm the migration and lamellipodial defect in

1008 Extended Data Fig. 3a-b) and *RHOJ*-specific (TRCN0000047606) shRNAs were either used

1009 in the pLKO.1 vector or subcloned into the pLVX-shRNA2 vector (No. PT4052-5; Clontech,

1010   Westburg BV, Leusden, the Netherlands). Scrambled shRNAs or the empty vectors were

1011   used as negative controls (both with the same outcome). All constructs were sequence veri-

1012   fied. Lentiviral particles were produced in 293T cells as previously described [2].

1013   **RECOMBINANT PROTEIN PRODUCTION:** Template vectors pRRLhGS, pRRLhGS^{R324C} and

1014   pRRLhGS^{R341C} containing the gene encoding wild type or point mutated human *GS* were

1015   used as templates for PCR-based cloning. Recombinant constructs were expressed in the

1016   *Escherichia coli* strain BL21 codon + pICA2 that was transformed with pLH36-hGS in which

1017   expression is induced by isopropyl b-D-1-thiogalactopyranoside under control of a pL-

1018   promotor developed by the Protein Core of VIB (WO 98/48025, WO 04/074488). The pLH36

1019   plasmid is provided with a His$_6$-tag followed by a murine caspase-3 site. The murine caspase-

1020   3 site can be used for the removal of the His$_6$-tag attached at the N-terminus of the protein of

1021   interest during purification. The transformed bacteria were grown in 200 ml Luria Bertani me-

1022   dium supplemented with ampicillin (100 µg ml^{-1}) and kanamycin (50 µg ml^{-1}) overnight at 28°C

1023   before 1/100 inoculation in a 20 l fermenter provided with Luria Bertani medium supplemented

1024   with ampicillin (100 µg ml^{-1}) and 1 % glycerol. The initial stirring and airflow was 200 rpm and

1025   1.5 l min^{-1}, respectively. Further, this was automatically adapted to keep the pO$_2$ at 30 %. The

1026   temperature was kept at 28°C. The cells were grown to an optical density of A$_{600nm}$ = 1.0,

1027   transferred at 20°C, and expression was induced by addition of 1 mM isopropyl b-D-1-

1028   thiogalactopyranoside overnight. Cells were then harvested and frozen at -20°C. After thaw-

1029   ing, the cells were resuspended at 3 ml g^{-1} in 50 mM Hepes pH 7.5, 500 mM NaCl, 20mM im-

1030   idazole, 1 mM phenyl-methylsulfonyl fluoride, 10 % glycerol, 5 mM β-mercaptoethanol, 1 mg

1031   per 100 ml DNAseI (Roche) and 1 tablet per 100 ml Complete Protease Inhibitor (Roche).

1032   The cytoplasmic fraction was prepared by using the Emulsiflex followed by centrifugation. All

1033   steps were conducted at 4°C. The clear supernatant was applied to a 20 ml Ni-Sepharose 6

1034 FF column (GE Healthcare), equilibrated with 50 mM Hepes pH7.5, 500 mM NaCl, 20mM im-

1035 idazole, 10 % glycerol, 5 mM β-mercaptoethanol and 1 mM phenyl-methylsulfonyl fluoride.

1036 The column was eluted with 50 mM Hepes pH 7.5, 500 mM NaCl, 400 mM imidazole, 10 %

1037 glycerol, 5 mM β-mercaptoethanol and 1 mM phenyl-methylsulfonyl fluoride after an interme-

1038 diate elution step with 50 mM imidazole in the same buffer. Finally, the elution fraction was

1039 injected on a HiLoad 26/60 Superdex prep grade with 20 mM Hepes pH 7.5, 300 mM NaCL,

1040 10 % glycerol and 0.5 mM TCEP as running solution. The obtained elution fractions were

1041 analyzed by SDS-PAGE. Recombinant protein concentration was determined using the Mi-

1042 cro-BCA assay (Pierce).

1043 *IN VITRO* KNOCK-DOWN/OVEREXPRESSION STRATEGIES: To minimize off-target effects and other

1044 silencing artifacts, key findings were confirmed with at least two independent and validated

1045 *GS*-specific shRNAs (see above) and appropriate controls or with a *GS*-specific siRNA duplex

1046 (5'-GGAAUAGCAUGUCACUAAAGCAGGC-3') and scrambled control (TriFECTa™, IDT). For

1047 lentiviral transduction of shRNAs or overexpressing constructs an MOI of 10 or 5 was used,

1048 respectively. In case of simultaneous transduction of 2 different shRNAs, a MOI 7.5 was used

1049 for each individual shRNA. In case of simultaneous transduction of a shRNA in combination

1050 with an overexpression construct, the shRNA was transduced at MOI 10 and the overexpres-

1051 sion construct at MOI 5, except for overexpression constructs for shRNA-resistant *GS* which

1052 were transduced at MOI 2.5. Transductions were performed on day 0 in the evening, cells

1053 were refed with fresh medium on day 1 in the morning and experiments were performed from

1054 day 3 or 4 onwards. siRNA transfection mixtures (in a total volume of 500 µl) were prepared in

1055 Opti-MEM containing GlutaMAX-I (Invitrogen) with Lipofectamine RNAi Max transfection rea-

1056 gent (Invitrogen, Belgium) according to the manufacturer's instructions. The mixtures were

1057 added to the cells (150,000 cells in 6 well-format plate) together with 2 ml EBM2 without anti-

1058 biotics for overnight transfection after which the medium was changed back to the regular

1059 M199 culture medium. siRNA transfection was done at least 48 h prior to functional assays.

1060 BiFC plasmids were transfected into HEK293A cells with Fugene® HD transfection reagent

1061 following the manufacturer's guidelines. KD efficiency and overexpression levels were closely

1062 monitored for each experiment either on mRNA (QRT-PCR) or protein level.

1063 **RNA ISOLATION AND GENE EXPRESSION ANALYSIS:** Total RNA was extracted with Invitrogen's

1064 PureLink RNA mini kit according to the manufacturer's instructions; quality and quantity were

1065 measured on a Nanodrop (Thermo Scientific). cDNA synthesis was performed with the iScript

1066 cDNA synthesis kit (BioRad). Quantitative RT-PCR analyses were performed as previously

1067 described [1] on an Applied Biosystems 7500 Fast device with in house-designed primers and

1068 probes or premade primer sets (Applied Biosystems or Integrated DNA Technologies) for

1069 which sequences and/or primer set ID numbers are available upon request. *ENOX2* or *HPRT*

1070 were used as housekeeping genes.

1071 **WESTERN BLOTTING AND (CO-)IMMUNOPRECIPITATION:** Proteins were extracted in Laemmli buffer

1072 (125 mM Tris-HCl (pH 6.8), 2% SDS,10% glycerol) or in RIPA buffer (25 mM Tris-HCl (pH

1073 7.6), 150 mM NaCl, 1% NP-40, 1% sodium deoxycholate, 0.1% SDS) containing protease

1074 and phosphatase inhibitor mixes (Roche Applied Science). After shearing of genomic DNA,

1075 proteins in the lysates were separated by SDS-PAGE, transferred to nitrocellulose or polyvi-

1076 nylidene difluoride membranes and detected with specific antibodies and HRP-conjugated

1077 secondary antibodies in combination with ECL or SuperSignal Femto Western blotting sub-

1078 strate (Thermo Scientific). Densitometric quantification was done with ImageJ. For MLC and

1079 pMLC immunoblotting, each sample was loaded on two separate gels. One gel was used to

1080 detect MLC and the second was used to detect pMLC. Both gels had their own loading con-

1081   trol, namely α-tubulin. pMLC/MLC was quantified as follows: (pMLC/α-tubulin)/(MLC/α-

1082   tubulin). Membrane *versus* cytosolic protein fractions were purified with the Plasma Mem-

1083   brane Protein Extraction Kit (101Bio) according to the manufacturer's guidelines and using

1084   proprietary buffers. For co-immunoprecipitation (co-IP) of endogenous or overexpressed pro-

1085   teins, ECs were lysed by rotating at 4°C during at least 4 h in co-IP lysis buffer (20 mM Tris-

1086   HCl pH8, 137 mM NaCl, 10% glycerol, 1% nonidet NP-40 and 2 mM EDTA). Equal amounts

1087   of protein were incubated overnight with specific antibodies or matching isotype control IgGs

1088   at 4 °C. Subsequently, 20 µl of protein A/G-Sepharose beads was added to the immune com-

1089   plexes for 4 h at 4°C under gentle rotation. The beads were pelleted, washed three times with

1090   ice-cold co-IP lysis buffer and boiled for 5 min in reducing agent and loading buffer prior to

1091   SDS-PAGE. To determine the impact of deleting RHOJ's first 20 N-terminal AAs on the inter-

1092   action with GS, co-IPs were done as above on ECs simultaneously overexpressing GS and

1093   RHOJ-EGFP or ΔN20-RHOJ-EGFP. In some of the experiments the expression of the ΔN20-

1094   RHOJ-EGFP was lower than the expression of RHOJ-EGFP. To correct for this possible bias,

1095   densitometric quantification of all bands was performed in ImageJ and signals in the IP lanes

1096   were normalized to the input signals. The amount of GS IP'ed was the same in the RHOJ-

1097   EGFP and ΔN20-RHOJ-EGFP condition (data not shown).

1098   **BIOCHEMICAL AND METABOLIC ASSAYS:** *BICINCHONINIC ACID (BCA) ASSAY* (Pierce) was used to

1099   determine protein content. *LDH RELEASE* as a measure for cell survival was determined with

1100   the Cytotoxicity Detection Kit (Roche Applied Science). *INTRACELLULAR REACTIVE OXYGEN SPE-*

1101   *CIES (ROS) LEVELS* were determined by CM-H_2DCFDA dye (Invitrogen) labeling following

1102   manufacturer's guidelines. *GLUTAMINE SYNTHETASE ACTIVITY* in living cells. The enzyme activity

1103   in living cells was determined by pulse-labeling the cells for 30 min with 2 mM $^{15}NH_4Cl$ and

1104   subsequent determination of ^{15}N incorporation in intracellular glutamine by gas chromatog-

1105   raphy - mass spectrometry GC-MS (see below). Similarly, GS activity was measured by

1106   pulse-labeling for 30 min with 0.5 mM [U-^{13}C]-glutamic acid and subsequent tracing of ^{13}C in-

1107   to glutamine by GC-MS. The 0.025 mM glutamine condition was added to this assay for the

1108   sole purpose of having a positive control – lowering external glutamine levels should increase

1109   GS activity – and are not in any way reflecting maximal GS activity. Background signals were

1110   determined by pre-incubating the cells with the GS inhibitor MSO. As an independent manner

1111   (not relying on labeling one of the immediate substrates (NH_4^+ or glutamate)) to determine GS

1112   activity, we performed steady state labeling of ECs with [U-^{13}C]-glucose (5.5 mM) and deter-

1113   mined carbon contribution to α-ketoglutarate, glutamate and glutamine (for labeling scheme

1114   see Extended Data Fig. 5f). Prior to derivatization for GC-MS analysis, cells were washed

1115   with ice-cold 0.9% NaCl and extracted in ice cold 80/20 methanol/water. GLUTAMINE UPTAKE

1116   ASSAY: Dynamic [U-^{13}C]-glutamine uptake assays were performed as follows: 2.5 x 10^5

1117   cells/well were seeded in 6 well plates and pulse-labeled for 0, 10, 20 and 30 min with the

1118   regular M199 culture medium containing 0.6 mM [U-^{13}C]-glutamine instead of the regular 0.6

1119   mM unlabeled glutamine. The 0 min time point represents an absolute negative control for

1120   which extracts were made from ECs that were never treated with tracer-containing medium.

1121   For the 0.5 min time point, the labeled medium was put on the cells and immediately aspirat-

1122   ed (all together taking 0.5 min). At all time points, cells were thoroughly washed twice with

1123   ice-cold 0.9% NaCl to ensure complete removal of tracer-containing medium. Cellular extracts

1124   were then made in ice-cold 80/20 methanol/water, prior to derivatization for GC-MS meas-

1125   urements. Alternatively, cells were incubated with 0.5 μCi ml^{-1} [U-^{14}C]-L-glutamine for 10 min

1126   after which they were washed at least three times with ice-cold PBS. The last PBS wash was

1127   collected and checked for residual radioactivity. Cells were then lysed with 200 μl 0.2 N NaOH

1128   and lysates were neutralized with 20 μl 1N HCl and used for scintillation counting. [^{3}H]-

1129   *THYMIDINE INCORPORATION*: Proliferation was determined by labeling the cells with 1 µCi ml^{-1}

1130   [^{3}H]-thymidine for 2 h, followed by fixation in 100% ethanol for 15 min, precipitation with 10%

1131   trichloroacetic acid and finally lysis in 0.1 N NaOH. Scintillation counting was used to assess

1132   the amount of [^{3}H]-thymidine incorporated into the DNA. *ENERGY CHARGE ASSESSMENT:* 1.5 x

1133   10^6 cells were collected in 100 µl ice cold 0.4 M perchloric acid containing 0.5 mM EDTA. pH

1134   was adjusted with 100 µl of 2 M K$_2$CO$_3$. 100 µl of the mixture was subsequently injected onto

1135   an Agilent 1260 HPLC with a C18-Symmetry column (150 x 4.6 mm; 5 mm; Waters), thermo-

1136   stated at 22.5 °C. Flow rate was kept constant at 1 ml min^{-1}. A linear gradient using solvent A

1137   (50 mM NaH$_2$PO$_4$, 4 mM tetrabutylammonium, adjusted to pH 5.0 with H$_2$SO$_4$) and solvent B

1138   (50 mM NaH$_2$PO$_4$, 4 mM tetrabutylammonium, 30% CH$_3$CN, adjusted to pH 5.0 with H$_2$SO$_4$)

1139   was accomplished as follows: 95% A for 2 min, from 2 to 25 min linear increase to 100% B,

1140   from 25 to 27 min isocratic at 100% B, from 27 to 29 min linear gradient to 95% A and finally

1141   from 29 to 35 min at 95% A. ATP, ADP and AMP were detected at 259 nm. *SEAHORSE EXTRA-*

1142   *CELLULAR FLUX MEASUREMENTS*: ECs were seeded at 1.5 x 10^5 cells per well on Seahorse

1143   XF24 tissue culture plates (Seahorse Bioscience Europe). Oxygen consumption (OCR)

1144   measurements were performed at 6 min intervals (2 min mixing, 2 min recovery, 2 min meas-

1145   uring) in a Seahorse XF24 device. Consecutive treatments with oligomycin (1.2 µM final),

1146   FCCP (5 µM final) and antimycin A (1 µM final) were performed to allow quantification of ATP-

1147   coupled OCR (OCR$_{ATP}$) and maximal respiration, next to basal OCR (OCR$_{bas}$). *GLYCOLYTIC*

1148   *FLUX:* ECs were cultured for 6 h in medium containing 0.4 mCi ml^{-1} [5-^{3}H]-D-glucose (Perkin

1149   Elmer) after which supernatant was transferred into glass vials sealed with rubber stoppers.

1150 ^{3}H$_2$O was captured in hanging wells containing a Whatman paper soaked with H$_2$O over a pe-

1151   riod of 48 h at 37 °C to reach saturation [1]. Then the paper was used for liquid scintillation

1152   counting. *^{14}C-GLUCOSE OXIDATION*: ECs were incubated for 6 h in medium containing 0.55 mCi

1153   ml^{-1} [6-^{14}C]-D-glucose. After that, 250 µl of 2 M perchloric acid was added to each well to stop

1154   cellular metabolism and to release $^{14}CO_2$, which was captured overnight at room temperature

1155   in 1x hyamine hydroxide-saturated Whatman paper. The radioactivity in the paper was deter-

1156   mined by liquid scintillation counting [1]. ^{14}C-GLUTAMINE OXIDATION: ECs were incubated for 6 h

1157   with medium containing 0.5 mCi ml^{-1} [U-^{14}C]-glutamine. 250 ml of 2 M perchloric acid was

1158   added to the cells to stop cellular metabolism and release $^{14}CO_2$. Trapping of $^{14}CO_2$ occurred

1159   as described above for glucose oxidation [1].

1160   **PROTEIN (AUTO)PALMITOYLATION DETECTION:** *IN VITRO PALMITOYLATION (CLICK REACTION-BASED)*:

1161   Purified bacterial GS protein was incubated with the indicated concentration of palmitoyl al-

1162   kyne-coenzyme A (Cayman Chemical) for 6 h at room temperature. The GS protein was then

1163   denatured by the addition of SDS. A click reaction with azide-biotin was performed to label the

1164   palmitoylated proteins [27]. Palmitoylated proteins were detected by SDS-PAGE followed by

1165   blotting with streptavidin-horseradish peroxidase. *FLUORESCENCE-BASED CoA RELEASE DETEC-*

1166   *TION*: During autopalmitoylation of proteins, palmitate is transferred from palmitoyl-CoA to the

1167   protein thereby releasing reduced CoA. α-Ketoglutarate dehydrogenase can use CoA to con-

1168   vert α-ketoglutarate to succinyl-CoA, a reaction that features reduction of NAD$^+$ to fluorescent

1169   NADH[31]. In brief, recombinant human GS was incubated with palmitoyl-CoA in MES buffer at

1170   physiological pH for at least 1 h at 30 °C. The volume was then adjusted to 200 µl in 50 mM

1171   sodium phosphate buffer (pH 6.8) containing 2 mM α-ketoglutaric acid, 0.25 mM NAD$^+$, 0.2

1172   mM thiamine pyrophosphate, 1 mM EDTA, 1 mM DTT and 32 mU α-ketoglutarate dehydro-

1173   genase. NADH levels were measured at 20 min after initiation of the reaction on a VICTOR

1174   plate reader (340 nm excitation – 465 nm emission). The experiment was performed in two

1175   directions: either with varying doses of palmitoyl-CoA for a fixed amount of recombinant GS or

1176   with varying amounts of recombinant GS for a fixed concentration of palmitoyl-CoA (40 µM).

1177   *AFFINITY CHROMATOGRAPHY*: A previously published protocol was used to determine cell-free

1178   binding of recombinant human GS to palmitoyl-CoA agarose[32]. A total of 50 µl of immobilized

1179   palmitoyl-CoA-agarose was equilibrated with 20 mM Tris·HCl (pH 8.4)/120 mM NaCl. The

1180   beads were incubated with 40 µg of recombinant human GS in a final volume of 200 µl for 2 h

1181   at room temperature on a rotatory system. Beads were pelleted and 20 µl of the supernatant

1182   was collected as the flow through (FT) fraction. Beads were then washed eight times with 500

1183   µl of 20 mM Tris·HCl (pH 8.4)/120 mM NaCl buffer. 20 µl of the last wash fraction was col-

1184   lected as fraction W8. Beads were then eluted with SDS loading buffer and heated for 15 min

1185   at 60 °C. 2 µg of recombinant protein was used as input fraction (IF). IF, FT, W8 and SDS-

1186   eluate were analysed by immunoblotting for GS. *IN CELL LABELING*: In cell labeling experi-

1187   ments were performed essentially as described previously [27]. HEK-293T cells were transfect-

1188   ed with the indicated expression plasmids. Twenty-four h after transfection, the medium was

1189   replaced with DMEM + 10% dialyzed FBS containing the indicated probes (50mM 16C-YA or

1190   50 mM 16C-BYA). After 18 h, cell lysates were collected by incubation of the cells on ice for

1191   15 min in lysis buffer (50 mM TEA-HCl (pH=7.4), 150 mM NaCl, 1% Triton X-100, 0.5% sodi-

1192   um deoxycholate, 0.1% SDS and 5 mM PMSF) followed by centrifugation for 10 min at

1193   15,000 *g*. Equal amounts of protein were then used for a click reaction with azide-biotin. For

1194   labeling with 17-ODYA, FLAG-RHOJ overexpressing ECs were incubated overnight with 17-

1195   ODYA (50 µM) in M199 supplemented with 3.6% fatty acid free BSA, 10% dialyzed FBS and

1196   5 mM sodium pyruvate. Cells were washed with ice-cold PBS and lysed in NaP lysis buffer

1197   (0.2 M $Na_2HPO_4.2H_2O$, 0.2 M $NaH_2PO_4.2H_2O$, 1 M NaCl, 10% NP40). 2 µg of anti-Flag anti-

1198   body was conjugated to 20 µl of dynabeads protein G (Thermofisher) for 1 h at RT. After

1199   washing the beads twice with NaP lysis buffer, at least 500 µg of protein was added to the

1200   beads for 3 h at 4°C. Then beads were washed 3 times with NaP lysis buffer and resuspend-

1201 ed in 20 µl of resuspension buffer (4% SDS, 50 mM TEA, 150 mM NaCl). The click reaction

1202 was initiated by adding 0.5 µl of 5 mM tetramethylrhodamine azide (TAMRA) (Lumiprobe), 0.5

1203 µl 50 mM tris (2-carboxyethyl)phosphine hydrochloride (TCEP-HCl), 0.5 µl 10 mM tris (1-

1204 benzyl-1*H*-1,2,3-triazol-4-yl) methyl]amine (TBTA) and 2,4 µl of 5 mM freshly made ascorbic

1205 acid. Samples were then incubated for 1 h at 37°C in the dark. Sample buffer (9.4 µl) and re-

1206 ducing agent (3.7 µl) were added to stop the reaction. After 10 min at room temperature in the

1207 dark, samples were frozen at -80°C or run on a 10% Bis-TRIS gel in MES buffer. STREPTAVI-

1208 DIN-PULLDOWN: After click reaction with azide-biotin, free azide-biotin was removed from the

1209 samples by centrifugal filtration column (Millipore). The samples were then incubated with

1210 streptavidin-conjugated beads for 1 h at room temperature. After washing with PBS-T, pro-

1211 teins were eluted from the beads by incubation in elution buffer (95% formamide, 10 mM

1212 EDTA (pH=8.0)) at 95°C for 5 min. ACYL-RESIN-ASSISTED CAPTURE (ACYL-RAC) in which free

1213 cysteine thiols are chemically blocked and palmitoylated cysteines are exposed and captured

1214 by a resin, was performed with the CAPTUREome™ S-Palmitoylated Protein Kit (Badrilla)

1215 with minor adaptations to the manufacturer's guidelines. 500 µg of protein were incubated for

1216 4 h in 500 µL of thiol blocking reagent (to block free thiols). Proteins were precipitated with

1217 ice-cold acetone and afterwards solubilized with 300 µL of binding buffer and spun down. Af-

1218 ter protein quantification, 30 µg was kept as total input fraction (IF), and equal amounts of pro-

1219 tein were incubated for 2.5 h with (or without to obtain the negative control preserved bound

1220 fraction (pBF)) a thioester linkage specific cleavage reagent to cleave the thioester bond.

1221 Newly liberated thiols were captured with CAPTUREome™ resin. The resin was spun down

1222 and the supernate was collected as the cleaved unbound fraction (cUF) to check if the pro-

1223 teins of interest were indeed completely depleted from the thioester cleavage reagent (mean-

1224 ing efficient capture of the free thiols by the resin). After thorough washing of the resin, cap-

1225   tured proteins (cleaved bound fraction (cBF)), were eluted with reductant and analyzed to-

1226   gether with the IF, cUF and pBF by SDS-PAGE followed by immunoblotting.

1227

1228   **GC-MS ANALYSIS:** Metabolites from cells were extracted in 800 µl 80% methanol (at -80 °C).

1229   Next the extracts were centrifuged at 4°C for 15 min at 20,000 x g and the supernatants were

1230   dried in a vacuum centrifuge. 25 µl of a 2% methoxyamine hydrochloride solution (20 mg dis-

1231   solved in 1 ml pyridine) was added to the dried fractions which were then incubated at 37 °C

1232   for 90 min. Then 75 µl of N-tert-butyldimethylsilyl-N-methyltrifluoroacetamide with 1% N-tert-

1233   butyldimethyl-chlorosilane (Sigma-Aldrich) was added and the reaction was carried out for 30

1234   min at 60°C. Reaction mixtures were centrifuged for 15 min at 20,000 x g at 4°C in order to

1235   remove insolubilities and the supernatant was transferred to a glass vial with conical insert

1236   (Agilent). GC-MS analyses were performed on an Agilent 7890A GC equipped with a HP-5

1237   ms 5% Phenyl Methyl Silox (30 m - 0.25 mm i.d. - 0.25 µm; Agilent Technologies) capillary

1238   column, interfaced with a triple quadrupole tandem mass spectrometer (Agilent 7000B, Ag-

1239   ilent Technologies) operating under ionization by electron impact at 70 eV. The injection port,

1240   interface and ion source temperatures were kept at 230 °C. Temperature of the quadrupoles

1241   was kept at 150°C. The injection volume was 1 µl, and samples were injected at 1:10 split ra-

1242   tio. Helium flow was kept constant at 1 ml min^{-1}. The temperature of the column started at 100

1243   °C for 5 min and increased to 260 °C at 2 °C min^{-1}. Next, a 40 °C min^{-1} gradient was carried

1244   out until temp reached 300 °C. After the gradient, the column was heated for another 3 min at

1245   325 °C. The GC-MS analyses were performed in Single Ion Monitoring (SIM) scanning for the

1246   isotopic pattern of metabolites.

1247   **LC-MS ANALYSIS:** *POLAR METABOLITES* were extracted using 250 µL of a 50-30-20 (methanol-

1248   acetonitrile-10 mM ammonium acetate pH 9.3 containing 2 µM of deuterated (d27) myristic

1249   acid as internal standard) extraction buffer. Following extraction, precipitated proteins and in-

1250   solubilities were removed by centrifugation at 20,000 x g for 20 min at 4 °C. The supernatant

1251   was transferred to the appropriate mass spectrometer vials. Measurements were performed

1252   using a Dionex UltiMate 3000 LC System (Thermo Scientific) in-line connected to a Q-

1253   Exactive Orbitrap mass spectrometer (Thermo Scientific). 15 µl of sample was injected and

1254   loaded onto a Hilicon iHILIC-Fusion(P) column (Achrom). A linear gradient was carried out

1255   starting with 90% solvent A (LC-MS grade acetonitrile) and 10% solvent B (10 mM ammonium

1256   acetate pH 9.3). From 2 to 20 minutes the gradient changed to 80% B and was kept at 80%

1257   until 23 min. Next a decrease to 40% B was carried out to 25 min, further decreasing to 10%

1258   B at 27 min. Finally, 10% B was maintained until 35 min. The solvent was used at a flow rate

1259   of 200 µl min^{-1}, the column's temperature was kept constant at 25 °C. The mass spectrometer

1260   operated in negative ion mode, settings of the HESI probe were as follows: sheath gas flow

1261   rate at 35, auxiliary gas flow rate at 10 (at a temperature of 260 °C). Spray voltage was set at

1262   4.8 kV, temperature of the capillary at 300 °C and S-lens RF level at 50. A full scan (resolu-

1263   tion of 140,000 and scan range of m/z 70-1050) was applied. For the data analysis, we used

1264   an in-house library and metabolites of interest were quantified (area under the curve) using

1265   the XCalibur 4.0 (Thermo Scientific) software platform.

1266   **IN VITRO ASSAYS:** *ENDOTHELIAL SPHEROID CAPILLARY SPROUTING* was performed following estab-

1267   lished protocols [1,2]. To form the spheroids, ECs were cultured overnight in hanging drops in

1268   EGM-2 medium with methylcellulose (Sigma-Aldrich; 20 %volume of a 1.2% solution of

1269   methylcellulose 4000 cP). Spheroid sprouting entails both EC proliferation and migration. To

1270   have a 'clean' view on the migration aspect in sprouting, we also included conditions in which

1271   we blocked EC proliferation prior to sprout formation. More in particular, mitotic inactivation

1272   was achieved by adding mitomycin C (1 µg ml^{-1}) to the medium. To induce sprouting, sphe-

1273   roids were embedded in a collagen gel and incubated for 20 h. If required, chemical com-

1274   pounds (Fasudil at 10 μM, H1152 at 1 μM and Y26732 at 10 μM) were added during the col-

1275   lagen gel incubation step. Spheroids were then fixed with 4% paraformaldehyde and imaged

1276   under phase contrast illumination with a Motic AE 31 microscope (Motic Electric Group Co

1277   Ltd) or a Leica DMI6000B microscope (Leica Microsystems). Phase contrast images were

1278   used to quantify the number of sprouts per spheroid and the total sprout length (cumulative

1279   length of all sprouts on a spheroid). Spheroid body circumference was measured to correct

1280   for differences in size of the spheroid. Per experiment (*ie* per individual HUVEC isolation) at

1281   least 10 spheroids per condition were analyzed. *SCRATCH WOUND ASSAYS*: 75,000 HUVECs

1282   were seeded in 24-well format and were allowed to reach confluency over the next 24 h. At

1283   time T0 the confluent monolayer was scratched with a 200 μl pipet tip and photographed. The

1284   cells were further incubated for the indicated times and photographed again at time point Tx.

1285   Gap area at T0 minus gap area at Tx was measured with ImageJ and expressed as % migra-

1286   tion distance. Per well, three non-overlapping regions along the scratch were analyzed. Much

1287   like the spheroid sprouting, scratch wound healing is a combined readout for EC migration

1288   and proliferation. Therefore, we also included conditions in which the ECs were pre-treated

1289   with mitomycin C (1 μg ml^{-1}) to rule out the effect of proliferation. *BOYDEN CHAMBER ASSAYS*:

1290   50,000 HUVECs were seeded on 0.1% gelatin-coated tranwells and allowed to adhere. Then,

1291   the transwells were washed and refed with medium containing only 0.1% FBS and placed in

1292   bottom wells containing medium with 5% FBS as a pro-migratory stimulus. 16 h later,

1293   transwells were processed and analysed for numbers of migrated cells. Pre-treatment with

1294   mitomycin C (see above) was applied. *VELOCITY OF RANDOM MOVEMENT* was assessed on HU-

1295   VECs that were sparsely seeded on glass bottom 24-well plates. Time-lapse movies were

1296   generated by confocal image acquisition at 4 min intervals. Velocity of movement was deter-

1297   mined by tracking nucleus position in function of time (μm h^{-1}) (Tracking Tool TM, Gradi-

1298   entech AB, Uppsala, Sweden). Per condition, on average 2 or 3 individual cells were traced in

1299   each biological repeat. *LAMELLIPODIAL AREA* was measured on sparsely seeded phalloidin-

1300   stained ECs with Leica MM AF morphometric analysis software (Leica Microsystems, Mann-

1301   heim, Germany) with in-house developed journals and is expressed in percent of total cell ar-

1302   ea. Treatment with MSO (1 mM), Y27632 (10 μM), Fasudil (10 μM), H1152 (1 μM), ML7 (15

1303 μM) and peptide 18 (15 μM) were done 24 h prior to analysis of the cells. Per experimental

1304   condition, a minimum of ten individual cells was analyzed. *STAINING AND QUANTIFICATION OF*

1305   *VE-CADHERIN JUNCTIONS:* VE-cadherin staining and quantification of junctional length and gap

1306   index was performed as previously described [33]. First, the total junctional length (100%) was

1307   determined by summing up all segments, then the sum of all continuous segments was calcu-

1308   lated as the percentage of total junctional length. The percentage difference between total

1309   and continuous represents the discontinuous length. Gap size index (intercellular gap ar-

1310   ea/cell number) was determined with the formula ([intercellular gap area/total cell area]

1311   ×1,000)/cell number. Junctional lengths, intercellular gap area, and total cell area were de-

1312   fined manually with ImageJ. For each condition, a minimum of 10 fields was quantified (10-15

1313   cells per field on average) per experiment, and data shown represent the mean of at least 3

1314   independent experiments. *TRANS ENDOTHELIAL ELECTRICAL RESISTANCE (TEER):* 50,000 ECs

1315   were seeded on 6.5 mm 0.1% gelatin-coated polyester transwells, 0.4 µm pore size (Costar

1316   ref. 3470, Sigma-Aldrich). The electrical resistance was measured with an Endhome-6 elec-

1317   trode (World Precisions Instruments) connected to an EVOM2 voltohmmeter (World Preci-

1318   sions Instruments). Gelatin-coated wells without cells were used to measure the intrinsic elec-

1319   trical resistance of the inserts for background subtraction. Measurements were performed

1320   every day for 4 consecutive days, with at least 2 measurements per condition.

1321 **ACTIN DYNAMICS AND RHO (KINASE) ACTIVITY ASSAYS:** *LATRUNCULIN WASH-OUT*: ECs were treated

1322 with latrunculin B (100 ng ml^{-1}) for 30 min and were then washed three times with culture me-

1323 dium. The cells were fixed at the indicated time points and stained with phalloidin to visualize

1324 actin stress fibers. *THE F-/G-ACTIN RATIO* in GS^{KD} *vs* control ECs was determined in 4% para-

1325 formaldehyde-fixed cells which were permeabilized for 10 min in PBS with 0.2% Triton X-100

1326 and stained with phalloidin-Alexa 488 and deoxyribonuclease I-Alexa 594 (1:200) [34]. Fluores-

1327 cence intensities were quantified with ImageJ and were based on gray values. On average,

1328 ten individual cells were analyzed per experimental condition. For *RHOJ ACTIVITY* measure-

1329 ments, cells were lysed in buffer containing 50 mM Tris, pH 7.6, 150 mM NaCl, 1% Triton X-

1330 100, 0.5 mM MgCl$_2$, protease inhibitors and 0.1 μg μl^{-1} biotinylated CRIB-peptide. After spin-

1331 ning down for 4 min at 14,000 rpm at 4°C, 50 μl streptavidin-coated beads were added to the

1332 lysates. Subsequently, samples were rotated for 30 min at 4°C, beads were washed 4 times

1333 in the above buffer after which they were boiled for 5 min in reducing agent and loading buffer

1334 [35]. As negative controls in this assay, we used lysates from RHOJ^{KD} ECs, a streptavidin

1335 beads only-condition and lysates in which the biotinylated CRIB-peptide was replaced by an

1336 irrelevant biotinylated protein (Fig. 4c). *RHOA/B/C ACTIVITY* was determined with GST-

1337 Rhotekin pull down assays following previously established protocols [36]. *ROCK ACTIVITY* was

1338 assayed by determining phosphorylation of the ROCK target myosin light chain 2 (MLC2) on

1339 Western Blot or by immunostaining. Fluorescence intensities from immunostainings were

1340 quantified with ImageJ and were based on gray values.

1341 **CONFOCAL AND HIGH RESOLUTION IMAGING:** *CONFOCAL IMAGING* was performed on a Zeiss LSM

1342 510 Meta NLO or Zeiss LSM 780 confocal microscope (oil objectives: x 40 with NA 1.3, x 63

1343 with NA 1.4, x 100 with NA 1.3) with ZEN 2011 software (Carl Zeiss, Munich, Germany). With-

1344 in individual experiments, all images across different experimental conditions were acquired

1345   with the same settings. *DORA RHOA BIOSENSOR FRET IMAGING*: RHOA activity was measured

1346   in living HUVECs by monitoring yellow fluorescent protein (YFP) FRET over donor cyan fluo-

1347   rescent protein (CFP) intensities as described previously [37]. In brief, a Zeiss Observer Z1 mi-

1348   croscope, with a Chroma 510 DCSP dichroic splitter, two Hamamatsu ORCA-R2 digital CCD

1349   cameras and an attached dual camera adaptor (Zeiss) controlling a 510 DCSP dichroic mir-

1350   ror, was used for simultaneous monitoring of CFP and YFP emissions using filter sets ET

1351   480/40 and ET 540/40m (Chroma Technology, Rockingham, USA), respectively. To excite the

1352   CFP donor, ET 436/20x and 455 DCLP dichroic mirror was used (Chroma). For FRET/CFP

1353   ratiometric processing, CFP and YFP images were processed using the MBF ImageJ collec-

1354   tion. The images were background-subtracted, aligned and a threshold was applied. Finally,

1355   the FRET/CFP ratio was calculated and a custom lookup table was applied to generate a col-

1356   or-coded image, in which white and red colors illustrate high and blue colors illustrate low

1357   RHOA activities. *BiFC IMAGING AND QUANTIFICATION*: BiFC was evaluated using a laser scan-

1358   ning microscope (Fluoview FV1000, Olympus, Tokyo, Japan) equipped with a UPLSAPO 60x

1359   Oil objective (NA1.35). Before imaging cells were fixed with 4 % (v/v) paraformaldehyde and

1360   stained with DAPI (1/1,000 dilution, Invitrogen). A 488-nm laser was used for exciting EGFP

1361   while DAPI was excited using a 405-nm laser. A DM405/488/559/635 polychroic mirror was

1362   used to guide the excitation lasers to the sample. Fluorescence images of fixed cells were

1363   acquired using a sampling speed of 4 μs pixel^{-1}. Emission light was collected at 430-470 and

1364   500-550 nm, for DAPI and PAGFP, respectively. The images were acquired with a pixel size

1365   of 207 nm (1024 x 1024 pixels). Quantification of expression efficiency was done using a

1366   home-built routine in Matlab®. *TIRF MICROSCOPY*: A home build setup based on an inverted

1367   microscope (IX83, Olympus) was used to detect single molecules under total internal reflec-

1368   tion (TIRF) mode. The setup was equipped with an Electron Multiplying-CCD cameras (Im-

1369   agEM C9100-13; Hamamatsu Photonics, Hamamatsu, Japan) and an APON 60XOTIRF ob-

1370   jective lens (NA 1.49, Olympus). The GS-mEos3.2 molecules were excited with a 561-nm line

1371   from a DPSS laser (200 mW; Coherent Inc., Santa Clara, California) and converted with a

1372   405-nm line from a diode laser (Cube, 100 mW; Coherent Inc., Santa Clara, California). Be-

1373   fore being expanded, the laser lines were combined using a 405bcm dichroic mirror. The la-

1374   ser lines were guided onto the sample by a dichroic mirror, z488/561/633rpc. The fluores-

1375   cence of the red of mEos3.2 form was detected through a long pass filter 572 (HQ572LP), in

1376   combination with a band pass filter HQ590M40-2P. All the filters were purchased from Chro-

1377   ma Inc. Time-lapse fluorescence images were recorded with continuous illumination at a 62.5

1378   Hz acquisition rate (16ms per frame). *SINGLE PARTICLE TRACKING (SPT)*: For calculation of sin-

1379   gle molecule coordinates the program 'Localizer' running from Matlab was used [38]. After local-

1380   ization, the positions of a molecule detected in consecutive frames are connected to recon-

1381   struct a trajectory using home-developed software in Matlab. Coordinates presented in con-

1382   secutive frames are linked to form a single trajectory when they uniquely appear in a distance

1383   smaller than 856 nm (corresponding to 8 pixels). Trajectories with at least 3 steps were ana-

1384   lyzed using variational Bayes single particle tracking analysis (vbSPT), a software package

1385   for analysis of single particle diffusion trajectories, where the diffusion constants switch ran-

1386   domly according to a Markov process [39].

1387   **MICE:** *GS^{ECKO} MICE*: To obtain inducible EC-specific GS knock-out mice, *GS$^{lox/lox}$* mice [40] were

1388   intercrossed with *VECadherin-Cre^{ERT2}* [41] or with *Pdgfb-Cre^{ERT2}* [42] mice and named GS^{vECKO}

1389   and GS^{pECKO} respectively. Correct Cre-mediated excision of the loxed *GS* segment in tamoxi-

1390   fen-treated GS^{ECKO} mice was confirmed via PCR analysis of genomic DNA (Extended Data

1391   Fig. 1d-e). *GENERATION OF GS$^{+/GFP}$ CHIMERAS*: Blastocysts were collected from superovulated

1392   C57BL/6 females at post-coital day 3.5 and were cultured for 5-8 days in ES cell culture me-

1393 dium consisting of Knockout DMEM medium (Invitrogen), with 2 mM L-glutamine, fetal bovine

1394 serum (Hyclone, ThermoScientific), MEM non-essential amino acids 100X (Invitrogen), 0.01

1395 mM β-mercaptoethanol (Sigma-Aldrich), 1 mM sodium pyruvate (Invitrogen), 100U ml^{-1} peni-

1396 cillin, 100μg ml^{-1} streptomycin, and 2,000 U ml^{-1} Leukemia Inhibitory Factor (Merck, Millipore).

1397 Afterwards, the inner cell mass was selectively removed from the trophectoderm, trypsinized

1398 and replated on a Mitomycin C-arrested MEF feeder monolayer. ES cells were fed every day

1399 and passaged every 2-4 days onto new feeder cells. *GS$^{+/GFP}$* ES cells (E14IB10 ES cell line) [6]

1400 were injected into C57BL/6 blastocysts and high chimeric pups were killed at P5 for detection

1401 of GFP in the retinal microvasculature.

1402 ***IN VIVO* MODELS:** *ANALYSIS OF DORSAL DERMAL BLOOD VESSEL NETWORK*: From E11.5 to E13.5 af-

1403 ter vaginal plug, GS^{vECKO} pregnant dams were treated with tamoxifen (50 mg kg^{-1}) by oral ga-

1404 vage. At E16.5 they were euthanized by cervical dislocation after which embryos were dis-

1405 sected from the uterus. Yolk sacs were collected, washed with PBS and used for genotyping

1406 of the embryos. The embryos were fixed for 10 min in 1% PFA prior to dissection of the dorsal

1407 skin. The epidermal and dermal layers were separated under a dissection microscope. Dis-

1408 sected back skins were permeabilized overnight (0.5% Triton X-100, 0.01% sodium deoxy-

1409 cholate, 1% bovine serum albumin, 0.02% sodium azide) prior to whole-mount immunostain-

1410 ing with CD31. To systematically analyze the same region for each embryo, 1 rectangular

1411 confocal image (1700 x 1100 μm) was taken at the anterior side of the skin specimen with the

1412 upper longer side of the rectangle placed on the midline. Within each rectangular picture the

1413 number of branch points was determined with the cell counter tool in ImageJ in 6 ROIs (250 x

1414 250 μm), 3 in the top half and 3 in the bottom half of the rectangle, not overlapping with the

1415 larger arteries and veins. *NEONATAL RETINAL ANGIOGENESIS*: EC-specific GS deletion was ob-

1416 tained by IP administration of tamoxifen (Sigma; 10 mg kg^{-1}; dissolved in 1:10 EtOH:oil solu-

1417 tion) once daily from P1 to P3 in GS^{vECKO} or once at P2 for GS^{pECKO}. For *in vivo* proliferation

1418 quantification, EdU (5-ethynyl-2′-deoxyuridine; Invitrogen) was injected IP 2 h before sacri-

1419 fice. Unless stated otherwise, retinas were isolated at P5 as previously described [43] and fixed

1420 in 2% PFA for 2 h. Isolectin B4 (IB4), EdU, NG2 and ColIV stainings were performed as pre-

1421 viously described [1,2]. Radial outgrowth of the vascular plexus, vascular area, branch points,

1422 number of filopodia and number of distal sprouts were analysed on isolectin IB4-stained reti-

1423 nas (see below) with Image J. Numbers of branch points and EdU$^+$ ECs were quantified in

1424 200 x 200 μm ROIs; per retina 12 ROIs were placed at the front of the vascular plexus and 8

1425 ROIs were placed more towards the center of the plexus. Filopodia and distal sprouts were

1426 quantified on ten high magnification (63x) images per retina, each representing approximately

1427 200 μm of utmost vascular front. For analysis of the retinal vasculature at P21 (3 week-old)

1428 and P42 (6 week-old) mice underwent the same tamoxifen treatment regimen as for analyses

1429 at P5. In addition, different tissues were collected from P42 mice for endoglin and CD34 stain-

1430 ing to study blood vessels in different vascular beds. OXYGEN INDUCED RETINOPATHY: Oxygen

1431 induced retinopathy (ROP) was induced by exposing C57BL/6 pups to 70% oxygen from P7-

1432 P12. Pups were then returned to normoxia and injected daily with 20 mg kg^{-1} MSO. At P17,

1433 pups were euthanized and eyes were enucleated, fixed in 4% PFA and retinal flatmounts

1434 were stained for isolectin B4 [2,3]. MSO-treated animals retained normal behavior notwithstand-

1435 ing observable weight loss. Mosaic tile images were captured using the inverted Leica

1436 DMI6000B epifluorescence microscope (Leica, Manheim, Germany) and analysis of the vas-

1437 cular tuft area (the complete retina was analyzed, no ROIs were used) and the vaso-

1438 obliterated area was performed with NIH Image J software and are expressed as percentage

1439 of the total retinal area. CORNEAL (MICRO-)POCKET ASSAY (CPA) to induce neovascularization of

1440 the avascular cornea was performed as previously described [44]. In brief, in the eyes of 8

1441   week-old C57BL/6 mice, a lamellar micropocket was dissected toward the temporal limbus to

1442   allow placing of basic fibroblast growth factor (bFGF)-containing pellet on the corneal surface.

1443   Five days after implanting the pellets, the mice were sacrificed, the eyes were enucleated and

1444   the corneas were excised and fixed in 70% ethanol prior to CD31 antibody staining. After

1445   staining, the corneas were flat-mounted and imaged on a Zeiss LSM 780 confocal micro-

1446   scope. CD31$^+$ area was measured in ImageJ after thresholding the signal and is expressed as

1447   % of total cornea area. Production of the pellets was done as previously described [44]. The

1448   pellets contained 20 ng bFGF and the concentration of MSO in the initial solution from which

1449   the pellets were made was 10 mM. *IMIQUIMOD-INDUCED SKIN INFLAMMATION:* Ten week old fe-

1450   male Balb/C mice received a daily topical dose of 5% imiquimod cream (62.5 mg) on their

1451   shaved backs for four days to induce skin inflammation [3]. 1 h after each administration of the

1452   cream, the same skin area was treated either with Vaseline® jelly or Vaseline® jelly containing

1453   MSO (low dose: 20 mg kg^{-1}; or high dose: 40 mg kg^{-1}). The MSO treatment did not affect bod-

1454   yweight of the mice. Skins and spleens were collected and fixed in 4% PFA. Paraffin sections

1455   of skins were stained for CD105 (R&D Systems) and H&E. Images were captured with a

1456   Leica DMI6000B microscope (Leica microsystems, Mannheim, Germany). Per animal, ten

1457   images representing different locations along the total length of the skin specimen were ana-

1458   lyzed for CD105$^+$ area. *MILES VASCULAR PERMEABILITY ASSAY:* 8 week old female Balb/c mice

1459   were treated for 3 consecutive days with 20 mg kg^{-1} day^{-1} MSO or with vehicle prior to injec-

1460   tion with 300 µl 0.5 % Evan's blue dye. The inflammatory irritant mustard oil (0.25 ml allyl

1461   isothiocyanate in 4.75 ml mineral oil) was applied on one of the ears with a cotton swab to in-

1462   duce vascular permeability. Mineral oil as a control was applied on the other ear. After 15 min,

1463   again mustard oil/mineral oil was applied on the ear for 30 min, after which the circulation was

1464   flushed with saline for 3 min and mice were perfused with 1 % PFA in 50 mM citrate buffer

1465   (pH=3.5) for 2 min. Ears were cut and minced in formamide and incubated at 55°C overnight

1466   to extract the Evan's blue from the tissue. Quantification of the dye was performed by a spec-

1467   trophotometrical optical density measurement at 620 nm. HEMATOLOGICAL PROFILING IN 6

1468   WEEK-OLD MICE was performed with a Cell Dyn 3700 device (Abbott Diagnostics) according to

1469   the manufacturer's guidelines. Plasma measurements for different liver/inflammation parame-

1470   ters were performed in the clinical laboratory of the university hospital of Leuven. Prior ran-

1471   domization was not applicable for any of the above mouse models given that all animal treat-

1472   ments were done in baseline conditions. No statistical methods were used to predetermine

1473   the sample size. For all mouse experiments, data analysis was done by researchers blinded

1474   to the group allocation. All animal procedures were approved by the Institutional Animal Care

1475   and Research Advisory Committee of the University of Leuven.

1476   **IN SILICO SCREENING FOR PALMITOYLATION SITES:** The human RHOJ protein sequence was

1477   screened for putative palmitoylation sites on the SwissPalm website [22] entering 'RHOJ' as the

1478   protein name.

1479   **MODELING AND SIMULATIONS:** The GS models were built starting from X-ray crystallographic

1480   structures retrieved from the Protein Data Bank (entry 2OJW for human GS and 1FPY for

1481   bacterial GS). All simulations were run with Gromacs 5.1.4[45] and the Amber FF14SB[46] force

1482   field, while palmitoyl-CoA was parametrized with GAFF and the point charges were calculated

1483   with Gaussian 09[47] at the Hartree-Fock level with a 6-31G* basis set. The different models

1484   were then embedded in a TIP3P water box, counter ions were added to ensure the overall

1485   charge neutrality. An initial 2,000 steps of steepest descent and 500 steps of conjugated gra-

1486   dient were applied to minimize the geometry and remove steric clashes, followed by 10 ns of

1487   isothermal-isobaric (NPT) equilibration. The Berendsen barostat was applied to keep the

1488   pressure around 1 atm, while the temperature of 300K was maintained throughout all the

1489   simulations with the V-rescale algorithm[48]. 500 ns long molecular dynamics production runs

1490   were carried out for all the systems in the canonical (NVT) ensemble, for a cumulative total of

1491   2.5 µs. The particle mesh Ewald (PME)-Switch algorithm was used for electrostatic interac-

1492   tions with a cut-off of 1 nm, and a single cut-off of 1.2 nm was used for Van der Waals interac-

1493   tions. Four simulations for human GS and two for *Salmonella typhimurium*'s GS were run by

1494   placing the CoA moiety close to the adenosine binding site and allowing different initial posi-

1495   tions for the palmitoyl tail. The CoA head invariably docked and remained tightly bound to the

1496   adenine binding site in all simulations. Among these, two favorable alternative arrangements

1497   (Extended Data Fig. 8b) for the tail were identified in both systems. In one of these confor-

1498   mations, the beginning of the palmitate tail (from the point of view of the CoA moiety) ap-

1499   proaches very closely the conserved CYS209 (human residue numbering, Conformation A in

1500   Extended Data Fig. 8b, details in Extended Data Fig. 8c), and in the other conformation (Con-

1501   formation B in Extended Data Fig. 8b, details in Extended Data Fig. 8d) it approaches the

1502   conserved Ser65 and 75.

1503   **STATISTICAL ANALYSIS:** Data represent mean±s.e.m. of pooled experiments unless otherwise

1504   stated. Scatters in bar graphs represent the values of independent experiments or individual

1505   mice. In case individual values are highly alike, scatter points overlap and may no longer be

1506   visible as individual points. n values represent the number of independent experiments per-

1507   formed or the number of individual mice phenotyped. Statistical significance between groups

1508   was calculated with one of the following methods. For comparisons to point-normalized data,

1509   a two-tailed one-sample *t*-test was used in GraphPad Prism7. For pairwise comparisons, two-

1510   tailed unpaired *t*-tests were used in GraphPad Prism7. For multiple comparisons within one

1511   data set, one-way ANOVA with Dunnett's multiple comparison (comparing every mean with

1512 the control mean rather than comparing every mean with every other mean) was used in

1513 GraphPad Prism7. Mixed model statistics (this test does not assume normality or equal vari-

1514 ance) was used with the experiment as random factor only in case confounding variation in

1515 baseline measurements between individual EC isolations (for each experiment, ECs were

1516 freshly isolated from individual human umbilicals) or mouse litters precluded the use of the

1517 above described statistical tests. For this, R and the *lme4* package were used; p-values were

1518 obtained with the Kenward-Roger F-test for small mixed effect model datasets. The variation

1519 in baseline precluded meaningful scattering of individual datapoints in corresponding bar

1520 graphs. Sample size for each experiment was not pre-determined. A p-value <0.05 was con-

1521 sidered significant.

1522 **DATA AVAILABILITY:** Fig.1, Fig. 4, Fig. 5, Extended Data Fig. 1, Extended Data Fig. 7 and Ex-

1523 tended Data Fig. 8 have associated raw data (uncropped blots and/or gel pictures) in Extend-

1524 ed Data Fig. 9. Any additional information required to interpret, replicate or build upon the

1525 Methods or findings reported in the manuscript is available from the corresponding author up-

1526 on request.

1527

1528

1529

1530 **REFERENCES UNIQUE TO THE METHODS SECTION**

1531
1532 27   Zheng, B., Zhu, S. & Wu, X. Clickable analogue of cerulenin as chemical probe to
1533   explore protein palmitoylation. *ACS Chem Biol* **10**, 115-121, doi:10.1021/cb500758s
1534   (2015).

1535   28   Martin-Ramirez, J., Hofman, M., van den Biggelaar, M., Hebbel, R. P. & Voorberg, J.
1536   Establishment of outgrowth endothelial cells from peripheral blood. *Nat Protoc* **7**, 1709-
1537   1715, doi:10.1038/nprot.2012.093 (2012).

1538   29   Van Den Bosch, L., Vandenberghe, W., Klaassen, H., Van Houtte, E. & Robberecht,
1539   W. Ca(2+)-permeable AMPA receptors and selective vulnerability of motor neurons. *J*
1540   *Neurol Sci* **180**, 29-34 (2000).

1541   30   McKinney, S. A., Murphy, C. S., Hazelwood, K. L., Davidson, M. W. & Looger, L. L. A
1542   bright and photostable photoconvertible fluorescent protein. *Nat Methods* **6**, 131-133,
1543   doi:10.1038/nmeth.1296 (2009).

1544   31   Hamel, L. D., Deschenes, R. J. & Mitchell, D. A. A fluorescence-based assay to
1545   monitor autopalmitoylation of zDHHC proteins applicable to high-throughput screening.
1546   *Anal Biochem* **460**, 1-8, doi:10.1016/j.ab.2014.05.013 (2014).

1547   32   Kummel, D., Heinemann, U. & Veit, M. Unique self-palmitoylation activity of the
1548   transport protein particle component Bet3: a mechanism required for protein stability.
1549   *Proc Natl Acad Sci U S A* **103**, 12701-12706, doi:10.1073/pnas.0603513103 (2006).

1550   33   Fraccaroli, A. *et al.* Endothelial alpha-parvin controls integrity of developing vasculature
1551   and is required for maintenance of cell-cell junctions. *Circulation research* **117**, 29-40,
1552   doi:10.1161/CIRCRESAHA.117.305818 (2015).

1553   34   Ho, C. Y., Jaalouk, D. E., Vartiainen, M. K. & Lammerding, J. Lamin A/C and emerin
1554   regulate MKL1-SRF activity by modulating actin dynamics. *Nature* **497**, 507-511,
1555   doi:10.1038/nature12105 (2013).

1556   35   Timmerman, I. *et al.* A local VE-cadherin and Trio-based signaling complex stabilizes
1557   endothelial junctions through Rac1. *J Cell Sci* **128**, 3041-3054, doi:10.1242/jcs.168674
1558   (2015).

1559   36   van Buul, J. D. *et al.* RhoG regulates endothelial apical cup assembly downstream
1560   from ICAM1 engagement and is involved in leukocyte trans-endothelial migration. *J*
1561   *Cell Biol* **178**, 1279-1293, doi:10.1083/jcb.200612053 (2007).

1562   37   Heemskerk, N. *et al.* F-actin-rich contractile endothelial pores prevent vascular leakage
1563   during leukocyte diapedesis through local RhoA signalling. *Nat Commun* **7**, 10493,
1564   doi:10.1038/ncomms10493 (2016).

1565   38   Dedecker, P., Duwe, S., Neely, R. K. & Zhang, J. Localizer: fast, accurate, open-
1566   source, and modular software package for superresolution microscopy. *J Biomed Opt*
1567   **17**, 126008, doi:10.1117/1.JBO.17.12.126008 (2012).

1568   39   Persson, F., Linden, M., Unoson, C. & Elf, J. Extracting intracellular diffusive states
1569   and transition rates from single-molecule tracking data. *Nat Methods* **10**, 265-269,
1570   doi:10.1038/nmeth.2367 (2013).

1571   40   He, Y. *et al.* Glutamine synthetase deficiency in murine astrocytes results in neonatal
1572   death. *Glia* **58**, 741-754, doi:10.1002/glia.20960 (2010).

1573   41   Benedito, R. *et al.* The notch ligands Dll4 and Jagged1 have opposing effects on
1574   angiogenesis. *Cell* **137**, 1124-1135, doi:S0092-8674(09)00324-9 [pii]
1575   10.1016/j.cell.2009.03.025 (2009).

1576   42   Claxton, S. *et al.* Efficient, inducible Cre-recombinase activation in vascular
1577   endothelium. *Genesis* **46**, 74-80, doi:10.1002/dvg.20367 (2008).

1578   43   Pitulescu, M. E., Schmidt, I., Benedito, R. & Adams, R. H. Inducible gene targeting in
1579   the neonatal vasculature and analysis of retinal angiogenesis in mice. *Nat Protoc* **5**,
1580   1518-1534, doi:10.1038/nprot.2010.113 (2010).

1581   44   Kenyon, B. M. *et al.* A model of angiogenesis in the mouse cornea. *Invest Ophthalmol
1582   Vis Sci* **37**, 1625-1632 (1996).

1583   45   Abraham, M. J. *et al.* GROMACS: High performance molecular simulations through
1584   multi-level parallelism from laptops to supercomputers. *SoftwareX* **1**, 19-25 (2015).

1585   46   Maier, J. A. *et al.* ff14SB: Improving the Accuracy of Protein Side Chain and Backbone
1586   Parameters from ff99SB. *J Chem Theory Comput* **11**, 3696-3713,
1587   doi:10.1021/acs.jctc.5b00255 (2015).

1588   47   Frisch, M. *et al.* Gaussian 09, Revision C.01. Gaussian Inc., Wallingford CT. (2009).

1589   48   Bussi, G., Donadio, D. & Parrinello, M. Canonical sampling through velocity rescaling.
1590   *J Chem Phys* **126**, doi:Artn 014101
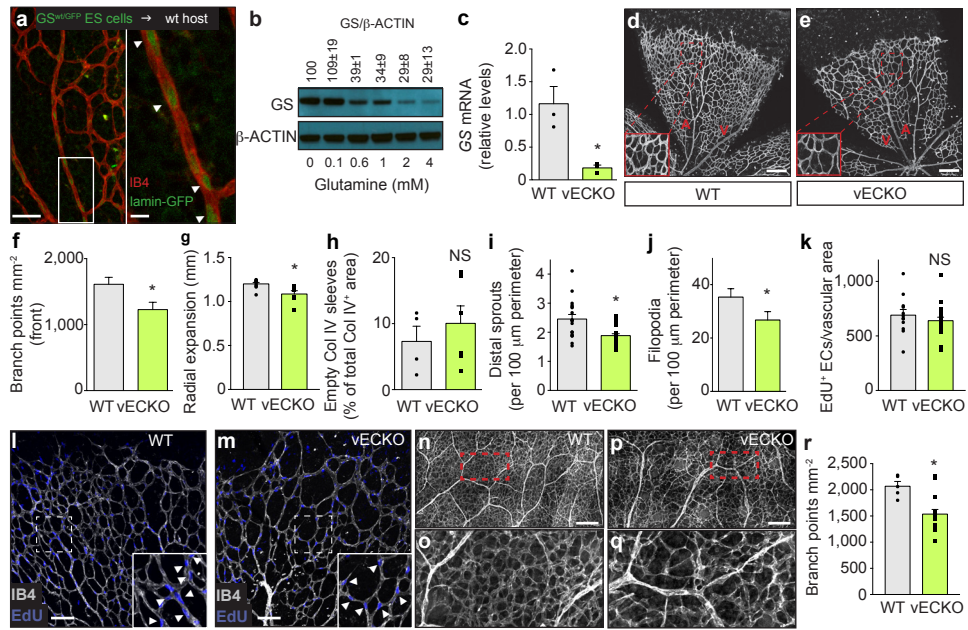1591   10.1063/1.2408420 (2007).
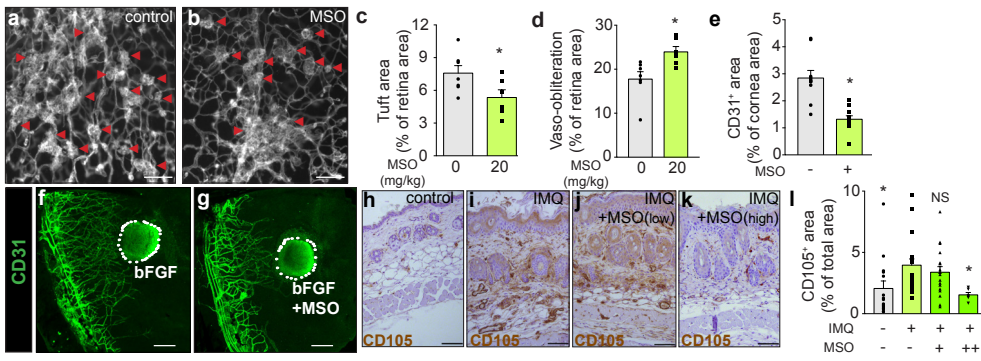
1592
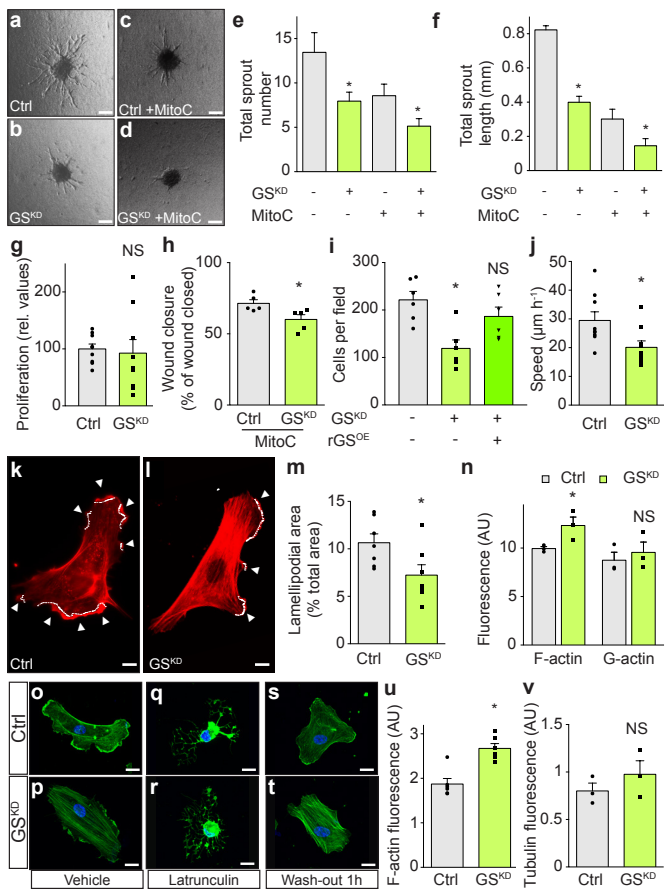

1593
1594
1595

1596

1597

1598

Figure 1

Figure 2

Figure 3
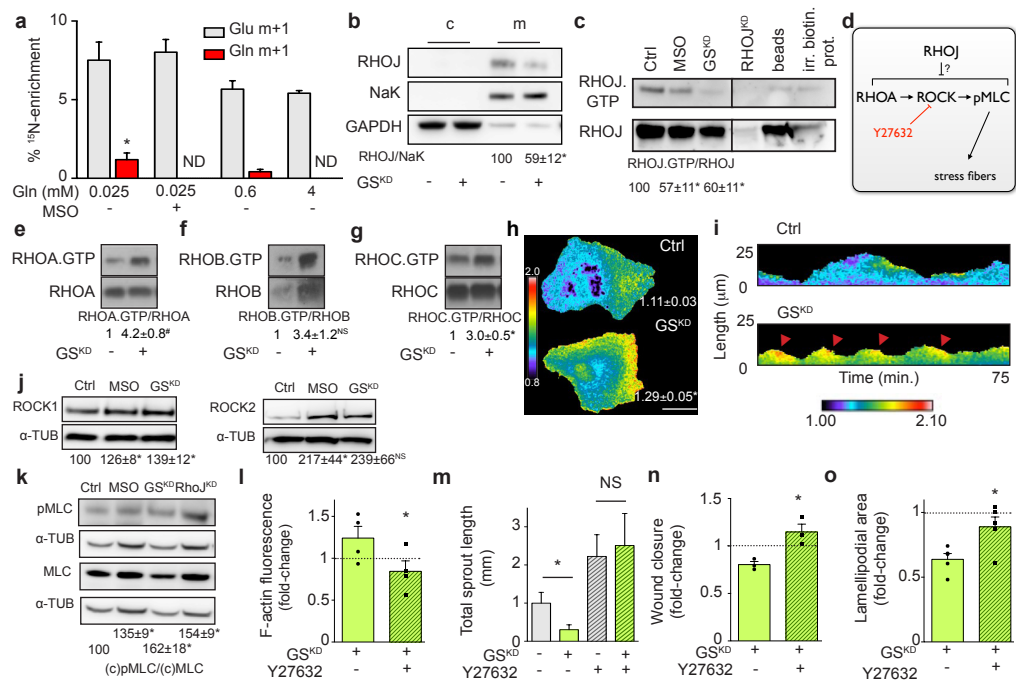
Figure 4

a
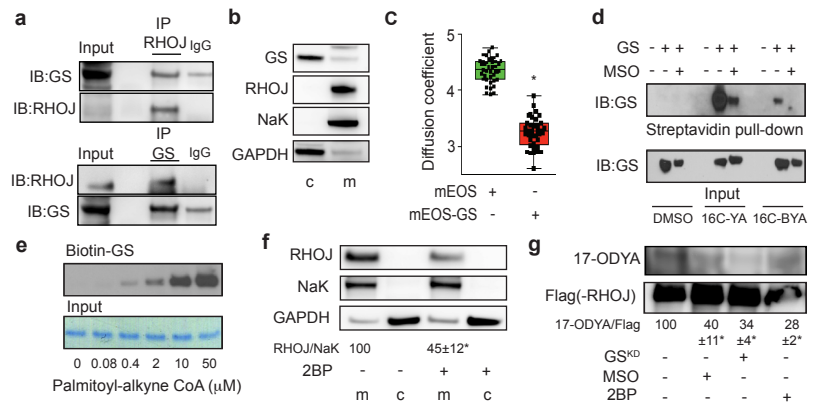
Input | IP RHOJ | IgG

IB:GS

IB:RHOJ

Input | IP GS | IgG

IB:RHOJ

IB:GS

b

GS

RHOJ

NaK

GAPDH

c | m

c

Diffusion coefficient

mEOS + | −
mEOS-GS − | +

d

GS − + + | − + + | − + +
MSO − − + | − − + | − − +

IB:GS

Streptavidin pull-down

IB:GS

Input

DMSO | 16C-YA | 16C-BYA

e

Biotin-GS

Input

0 0.08 0.4 2 10 50

Palmitoyl-alkyne CoA (μM)

f

RHOJ

NaK

GAPDH

RHOJ/NaK 100 | 45±12*
2BP − − + +
m c m c

g

17-ODYA

Flag(-RHOJ)

17-ODYA/Flag 100 | 40 ±11* | 34 ±4* | 28 ±2*
GSKD − − + −
MSO − + − −
2BP − − − +

Figure 5